Title

DETERMINATION OF aS FROM ENERGY-ENERGY CORRELATIONS IN e+e- ANNIHILATION AT 29 GeV

Author

Wood, D.R.

Publication Date

1987-10-01

Lawrence Berkeley Laboratory
UNIVERSITY OF CALIFORNIA

Physics Division

Determination of α_s from Energy-Energy Correlations in e^+e^- Annihilation at 29 GeV

D.R. Wood
(Ph.D. Thesis)

October 1987

Prepared for the U.S. Department of Energy under Contract DE-AC03-76SF00098

DISCLAIMER

DETERMINATION OF α_s FROM ENERGY-ENERGY CORRELATIONS IN e^+e^- ANNIHILATION AT 29 GEV

Darien Robert Wood
(Ph.D. Thesis)

Lawrence Berkeley Laboratory
University of California
Berkeley, California 94720

October 1987

This work was supported by the Director, Office of Energy Research, Office of High Energy and Nuclear Physics, Division of High Energy Physics of the U.S. Department of Energy under Contract Number DE-AC03-76SF00098.

DETERMINATION OF α_s FROM ENERGY-ENERGY CORRELATIONS IN e^+e^- ANNIHILATION AT 29 GEV

Darien Robert Wood

Abstract

We have studied the energy-energy correlation in e^+e^- annihilation into hadrons at $\sqrt{s}$=29 GeV using the Mark II detector at PEP. We find to $O(\alpha_s{}^2)$ that α_s=0.158±.003±.008 if hadronization is described by string fragmentation. Independent fragmentation schemes give α_s=.10-.14, and give poor agreement with the data. A leading-log shower fragmentation model is found to describe the data well.

In general, I wish to thank the entire Mark II collaboration. It was the efforts of these 140 physicist from ten institutions that made this experiment possible and provided a rich environment for my graduate education. In particular would like to thank my advisor Gerson Goldhaber along with George Trilling for their guidance, wisdom and humor. I am also grateful to Jonathan Dorfan for suggesting this thesis topic and for providing helpful advice on the analysis. I am greatly indebted to Alfred Petersen whose expertise in the fields of QCD and fragmentation was an invaluable resource for my thesis work. I also owe special thanks to John Haggerty for his guidance and instruction during the construction and installation phases of this project.

I have benefitted greatly from my association with fellow graduate students in the collaboration. I am indebted to many of them for many useful tips, patient instruction, lively discussions and friendship, and I thank Drew Baden, Peter Rowson, Bill Schmidke, and Paul Sheldon for being particularly helpful.

Finally, I am grateful to my family for their encouragement, support, and interest.

Table of Contents

Chapter 1. PREFACE 1

1.1 Organization 1

1.2 Quantum Chromodynamics 1

1.3 e^+e^- annihilation into hadrons 3

1.4 Energy-energy Correlation 8

Chapter 2. INTRODUCTION 11

Chapter 3. APPARATUS 13

Chapter 4. TRACK AND EVENT SELECTION 15

Chapter 5. ENERGY-ENERGY CORRELATION MEASUREMENT . . . 17

Chapter 6. α_s DETERMINATION 29

Chapter 7. MODEL COMPARISONS 37

Chapter 8. SUMMARY 39

Appendix A. APPARATUS (II) 41

A.1 The PEP Storage Ring 41

A.2 The Mark II Detector 41

A.2.1 History 41

A.2.2 General Description 42

A.2.3 Charged Particle Tracking 44

A.2.4 Calorimetry 47

Appendix B. Fragmentation Models 51

B.1 General Features 51

B.2 String Fragmentation 51

B.3 Independent Fragmentation Models 53

B.4 Shower Models 55

Appendix C. Details of Data Correction 58

C.1 General Method 58

C.2 Errors on C_1 and C_2 59

C.3 α_s dependence 64
Appendix D. Survey of Recent α_s Measurements 66
D.1 α_s measurements from the EECA 66
D.2 Other α_s measurements in e^+e^- experiments. 68
D.2.1 R Measurement 68
D.2.2 Quarkonium Decays 69
D.3 $\Lambda_{\overline{MS}}$ measurements in other types of experiments 69
D.3.1 Deep Inelastic Scattering 69
D.3.2 Two-photon Scattering 70
D.3.3 Hadron Collisions 71
D.4 Evidence of the running of α_s 71
REFERENCES 73

Chapter 1. PREFACE

1.1 ORGANIZATION

The body of this thesis, Chapt. 2 – Chapt. 8, is a journal article (LBL-23812, SLAC-PUB-4374, submitted to Physical Review D). It appears here exactly as it was submitted for publication, and it describes all of the key aspects of the work in a relatively concise manner. The article is written for an audience that is generally familiar with the theoretical and experimental issues involved. The introduction in Chapt. 2 is consequently quite brief. The remainder of this preface serves to supplement this with a more general discussion of the context of this work.

At the end of the thesis, four appendices are added. These provide some additional experimental and theoretical details along with a more general interpretation of the results.

1.2 QUANTUM CHROMODYNAMICS

The area of particle physics which we investigate here is the theory of the strong interaction, Quantum Chromodynamics (QCD). QCD is a renormalizable Lagrangian field theory based on an $SU(3)$ local gauge invariance. All quarks are assumed to possess fundamental $SU(3)$ "color" charges, and the color forces are mediated by vector bosons known as gluons. The couplings between gluons and quarks and among gluons themselves are described in lowest order by the Feynman vertices in Fig. 1.1. The constant g_s in the vertex factors determines the strength of the interactions, and the strong coupling constant is defined as

$$\alpha_s = \frac{g_s^2}{4\pi}. \tag{1.1}$$

This constant plays a role equivalent to that of α, the fine structure constant of Quantum Electrodynamics (QED).

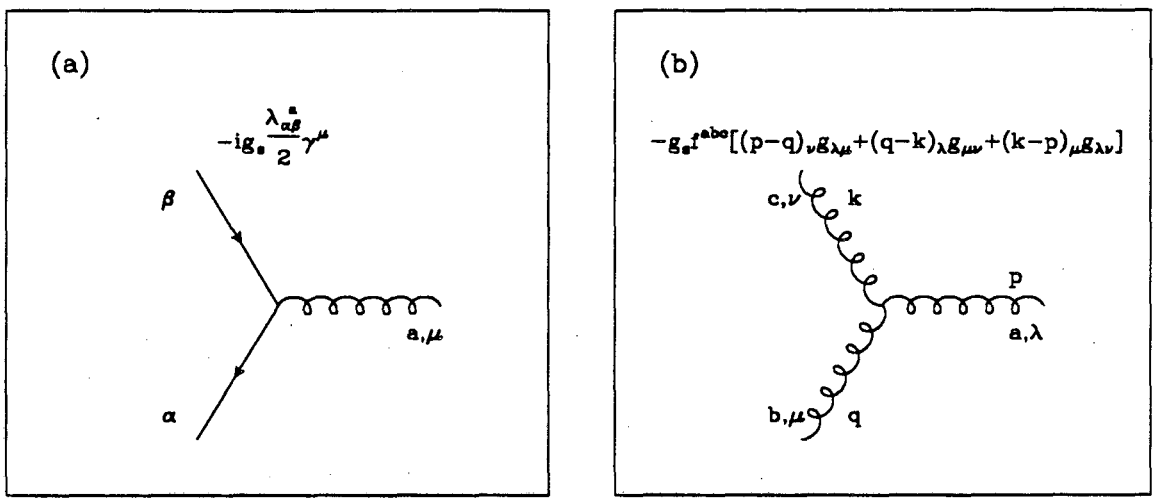

Figure 1.1 QCD vertex factors. *The lowest order Feynman diagrams for gluon couplings are show along with their vertex factors.*

QCD differs from QED is some important aspects. While in QED the coupling strength is small ($\alpha \ll 1$), this is not necessarily true in QCD. This is the fundamental statement of the "strong" character of the Strong Force. In addition, the value of α_s is sensitive to Q^2, the momentum scale of the interaction; we say α_s "runs" with Q^2. In the $\overline{MS}$ renormalization scheme (Modified Minimal Subtraction Scheme),[1] the Q^2 dependence of α_s is given by

$$\alpha_s = \frac{2\pi}{\frac{(33-2N_f)}{6}\ln\left(\frac{Q^2}{\Lambda^2}\right) + \frac{(153-19N_f)}{(33-2N_f)}\ln\left(\ln\left(\frac{Q^2}{\Lambda^2}\right)\right)}, \tag{1.2}$$

where N_f is the number of quark flavors open and Λ is the QCD scale parameter. This relation is shown in Fig. 1.2 for N_f=5 and $\Lambda_{\overline{MS}}$=300 MeV.

Also, as we see in Fig. 1.1(b), gluons are self-coupling. This is a consequence of the non-abelian nature of the $SU(3)$ gauge group, and it explains why α_s decreases with increasing Q^2. This sort of running of helps to explain two outstanding features of the strong interaction: asymptotic freedom and confinement. Asymptotic freedom states that at short distances (large Q^2) quarks within hadrons behave as loosely bound constituents, as is observed in deep inelastic scattering experiments. Confinement, on the other hand, requires that at large distances (small Q^2) colored objects such as quarks and gluons are never observed as free particles.

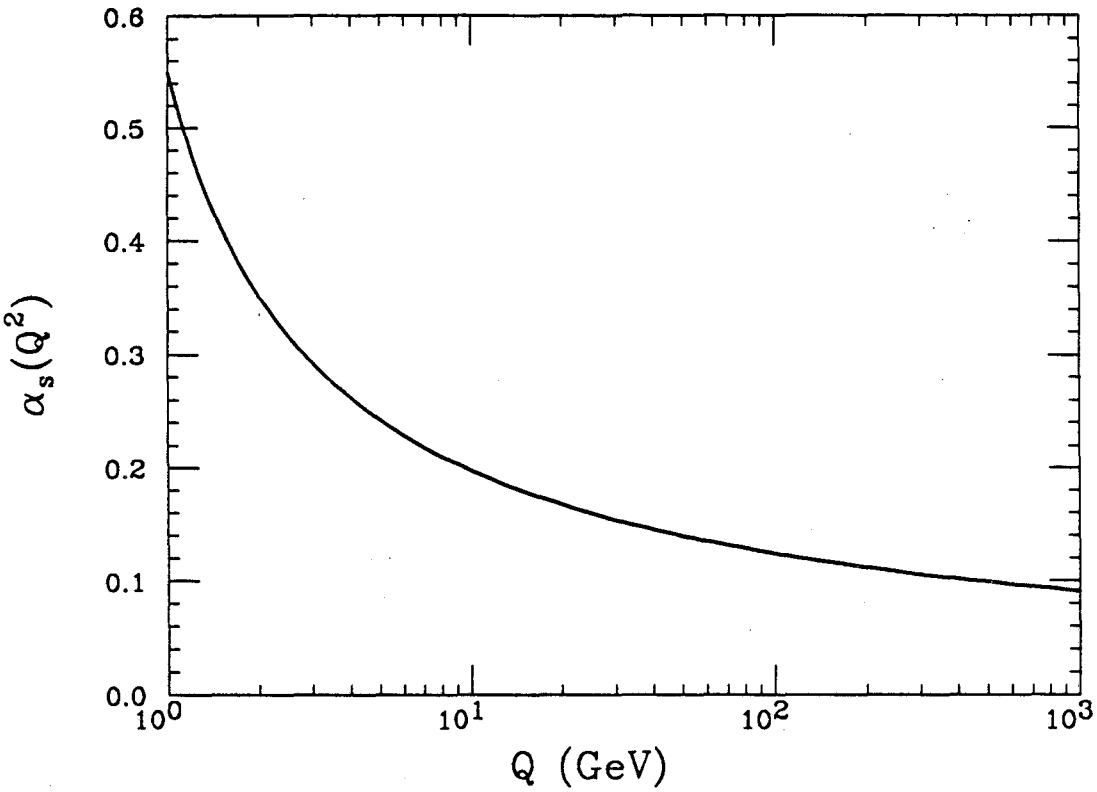

Figure 1.2 Momentum dependence of α_s. *The strong coupling constant, α_s, is shown as a function of momentum scale Q. We have assumed a value of $\Lambda_{\overline{MS}}$=300 MeV and five open quark flavors.*

QCD has been quite successful in explaining the qualitative features of a wide variety of hadronic interactions. No competing theory can claim the same success. Quantitative tests of QCD, however, are more difficult. The complications arise primarily from two sources. First, the relatively large size of α_s tends to make many low-order perturbative QCD calculations unreliable. Secondly, we do not observe quarks and gluons directly in experiments but rather we must infer their presence from the hadrons that they produce.

1.3 e^+e^- ANNIHILATION INTO HADRONS

The process $e^+e^- \rightarrow$ *hadrons* has proved to be one of the best tools for studying QCD. The experimental and theoretical considerations are simplified because the initial state is well-defined and free of strongly interacting particles. Examples of the simplest diagrams from hadronic production are shown in Fig. 1.3.

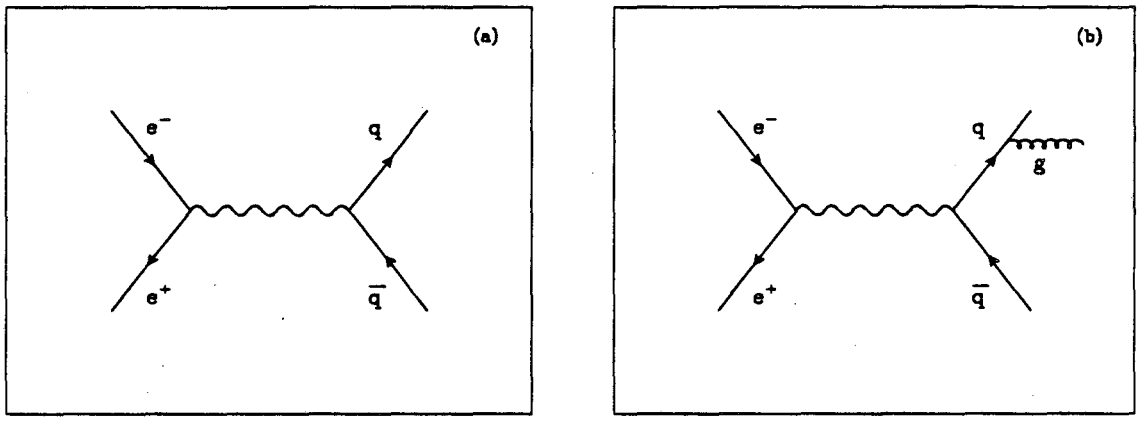

Figure 1.3 e^+e^- **Annihilation into Hadrons.** *The lowest order diagrams for (a)* $e^+e^- \rightarrow q\bar{q}$ *and (b)* $e^+e^- \rightarrow q\bar{q}g$.

At sufficiently high energies, the partons (quarks and gluons) manifest themselves as collimated jets of hadrons. Clean two-jet and three-jet events such as those in Fig. 1.4 and Fig. 1.5 provide some of the best qualitative evidence for the processes in Fig. 1.3.

A fundamental quantitative test of QCD in e^+e^- annihilation is the measurement of α_s. Naïvely, this can be accomplished simply by counting the relative numbers of two-jet and three-jet events and comparing this to the QCD prediction for two- and three-parton production rates. In practice, however, this is difficult because few three-jet events are as unambiguous as the example shown in Fig. 1.5.

In addition, the theoretical problems involved are not trivial. The slow convergence of the perturbative expansions in QCD suggests that $O(\alpha_s)$ calculations may be inadequate, so most precise quantitative tests require calculations to at least $O({\alpha_s}^2)$. Now we must include four-jet diagrams like Fig. 1.6(a) as well as virtual corrections to the three-jet and two-jet cross sections like Fig. 1.6(b) and (c). In all, about 30 distinct diagrams must be considered in the calculation.[2]

Aside from the sheer number of diagrams involved in calculating the $O({\alpha_s}^2)$ matrix element, there is the additional problem of divergences. As the energy of a gluon becomes small, or it becomes collinear with its parent quark, the production amplitude grows without limit. In the total cross section, these divergences in the three-parton and four-parton rates are cancelled by divergences in the vir-

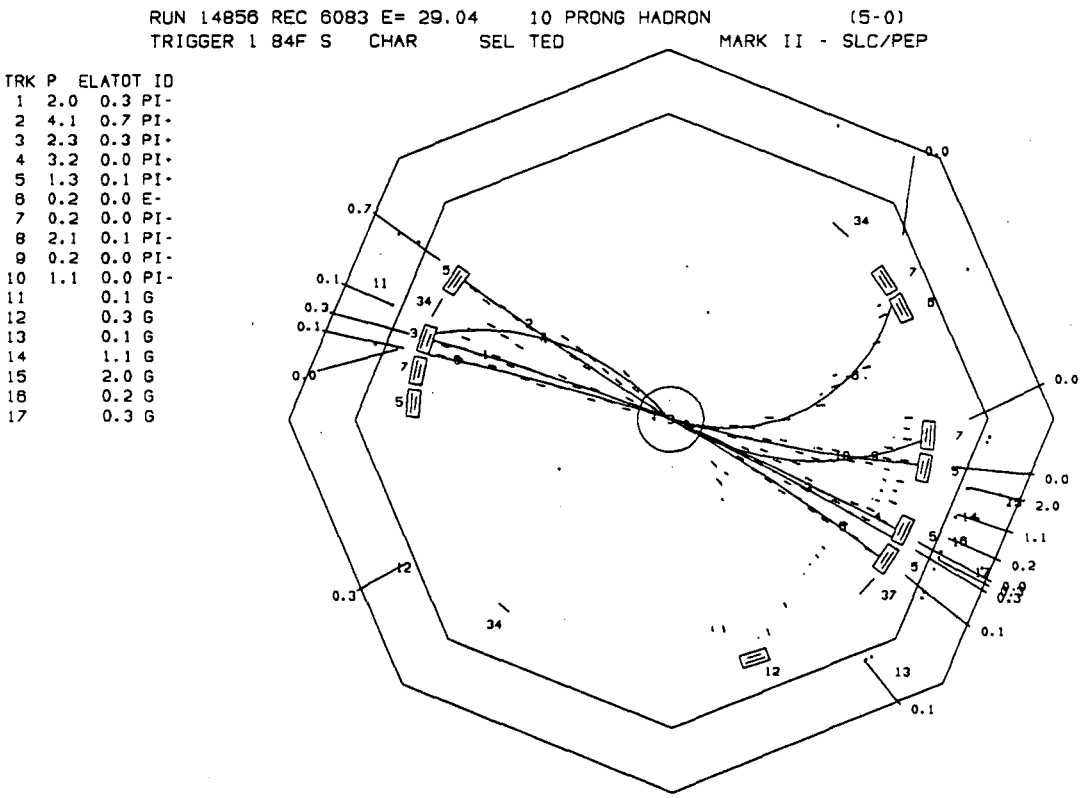

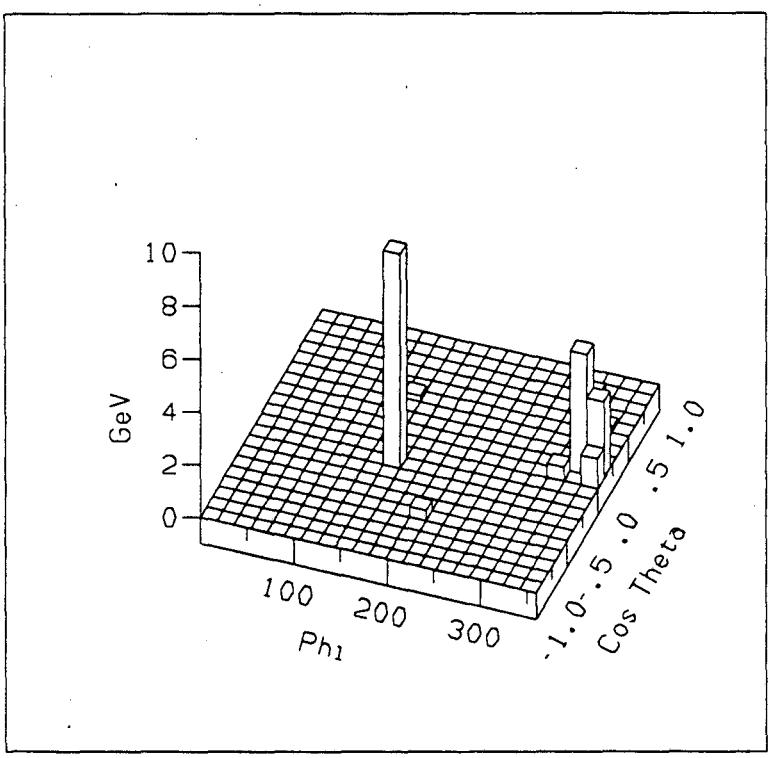

Figure 1.4 A two-jet event in the Mark II detector. *The "Lego" plot shows the detected charged plus neutral energy as a function of polar angle (θ) and asimuth (ϕ).*

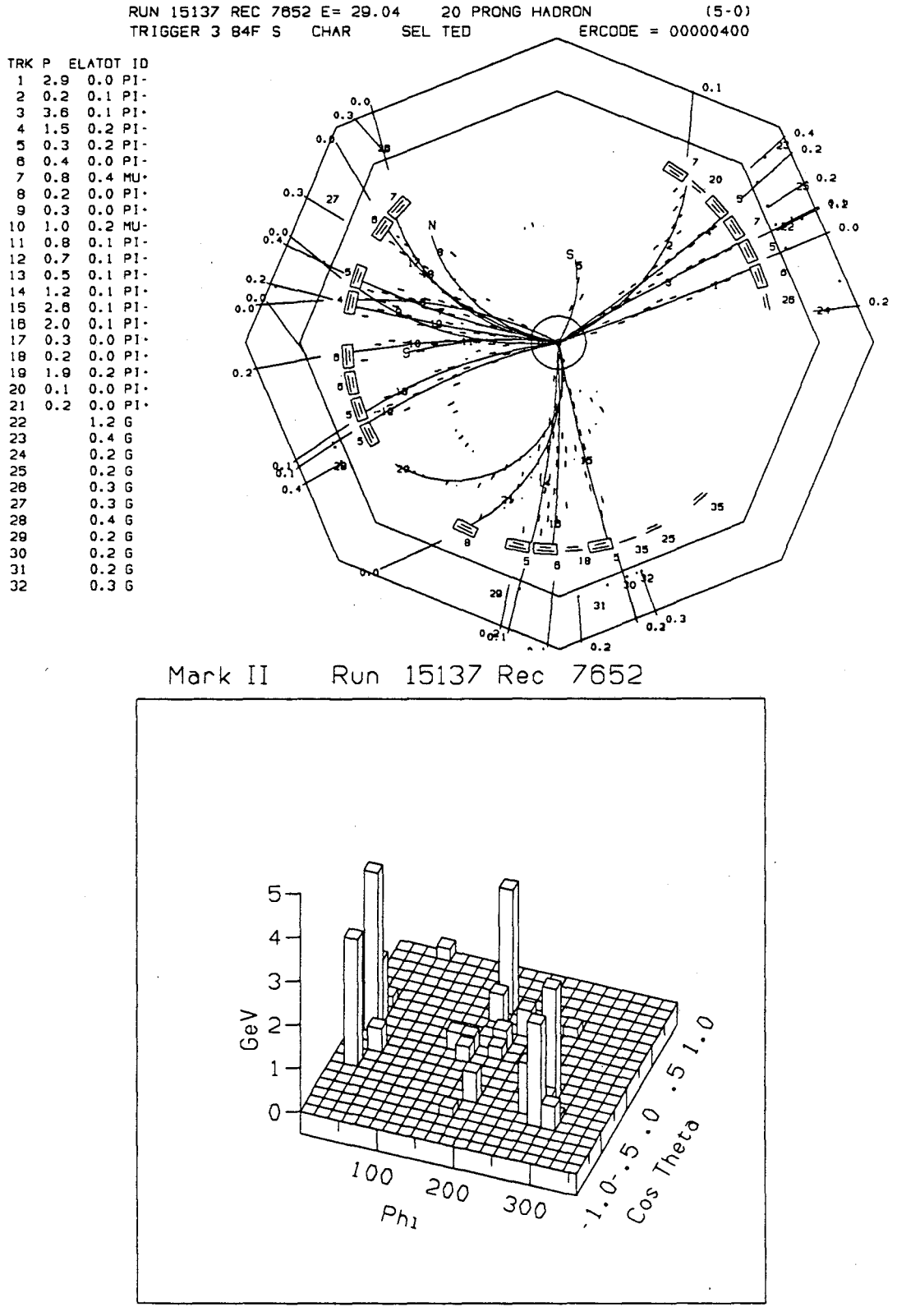

Figure 1.5 A three-jet event in the Mark II detector. *The "Lego" plot shows the detected charged plus neutral energy as a function of polar angle (θ) and azimuth (ϕ).*

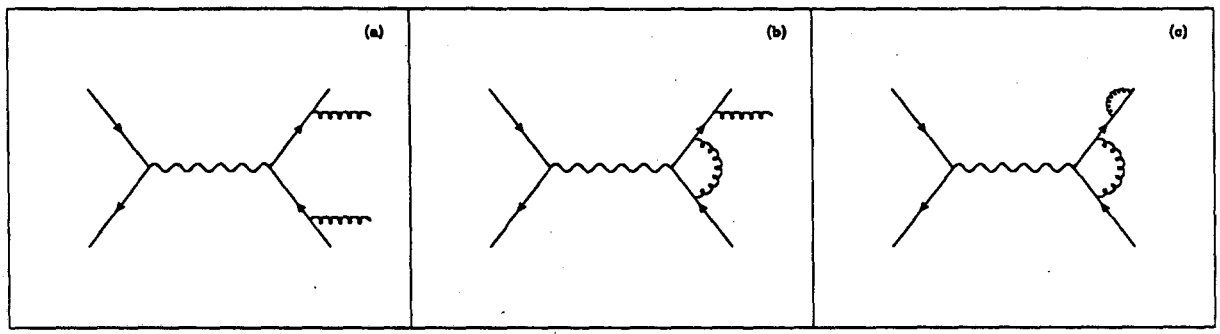

Figure 1.6 Higher order diagrams for $e^+e^- \rightarrow$ *hadrons*. *These are examples of diagrams which contribute at $O(\alpha_s{}^2)$ to the (a) four-jet cross section (b) three-jet cross section (c) two-jet cross section.*

tual corrections to the two-parton and three-partons cross sections, and a finite, unambiguous result is obtained. If we wish to compute the individual two-parton, three-parton, and four-parton cross sections, however, some sort of a cutoff scheme must be imposed. This is known as jet dressing.

A common method of jet dressing is to require that all pairs of partons have an invariant mass above some threshold. That is, for each pair of partons i and j in an event, the we check that $y_{ij} = (p_i + p_j)^2/s$ is greater than y_{min}. Then, for example, if two partons in a four-jet event fail this resolution test, the pair is replaced by a single parton and the event is treated as a three-jet event. Because a massless parton is substituted for a massive pair of partons, some algorithm must be employed to restore energy and momentum conservation. The threshold y_{min} should in principle be set at point where the individual partons cannot be resolved experimentally. This resolution criterion, however, is dominated by the hadronization process rather than any limitations of the apparatus. Thus, the choice of y_{min} is not clear, so it is desirable to study observables which are not particularly sensitive to this cutoff.

Several groups have calculated the $O(\alpha_s{}^2)$ matrix element for $e^+e^- \rightarrow$ *quarks+gluons*. Ellis, Ross and Terrano (ERT)[3] have computed it exactly in $4 + \nu$ space-time dimensions. For $\nu \neq 0$, the divergences vanish, and no cutoffs are needed.

To apply this calculation to a four dimensional world, however, we require that the terms depending on the cutoff parameter ν be transformed into functions of a more physical cutoff like y_{min}, as has been done by Kunstz.[5] Fabricius, Kramer, Schierholz and Schmitt (FKSS) performed an independent calculation of the dressed matrix element in which they applied physical resolution cuts from the outset. This result was later refined by Gutbrod, Kramer and Schierholz (GKS)[4] and this calculation was used by most of the experimental groups at PEP and PETRA. Most recently, Gottschalk and Shatz[6] have calculated the dressed matrix element where they handle the divergences differently and include important subleading corrections that are left out in the GKS and Kunstz calculations. These issues are discussed at length in Ref. 7 and 8.

1.4 Energy-Energy Correlation

In the present study, we use the Energy-Energy Correlation (EEC) to study the reaction $e^+e^- \rightarrow$ *quarks* + *gluons*. The EEC is an energy weighted angular correlation function defined by

$$\mathrm{EEC}(\chi) = \frac{1}{N} \sum_{events}^{N} \sum_{i} \sum_{j} \frac{E_i E_j}{E_{cm}^2} \delta(\chi - \chi_{ij}) \tag{1.3}$$

where i and j run over all particles (charged and neutral) in the event, and χ_{ij} is the angle between particles i and j. Note that the definition includes self-correlations terms ($i = j$), so the normalization relation $\int EEC(\chi) d\chi = 1$ holds if $\sum E_i = E_{cm}$. The energy-energy correlation asymmetry (EECA) is conventionally defined as

$$\mathrm{EECA}(\chi) = \mathrm{EEC}(180^\circ - \chi) - \mathrm{EEC}(\chi), \tag{1.4}$$

and is often weighted by $\sin\chi$ when it is plotted.

The sensitivity of these distributions to gluon radiation is easily shown by example. Figure 1.7 shows the EEC and EECA for the two-jet event pictured in Fig. 1.4. Note the large peaks in Fig. 1.7(a) near 0° (same jet correlations)

and 180° (opposite jet correlations). These largely cancel each other when the EECA (Fig. 1.7(b)) is formed. The distributions from a three-jet event look quite different, as seen in Fig. 1.8. In the EEC, the peak at 180° from back-to-back particles does not appear, and there are substantial contributions at intermediate angles ($\chi \sim 120°$). In addition, these contributions tend to persist in the EECA.

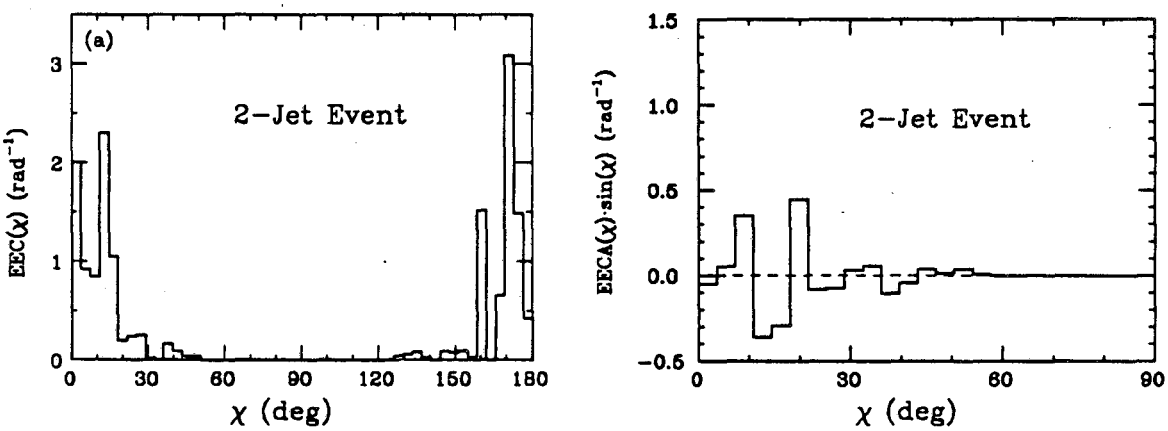

Figure 1.7 EEC and EECA for a two-jet event. *The EEC and EECA are shown for the two-jet event pictured in Fig. 1.4. The EECA has been weighted by* $\sin\chi$.

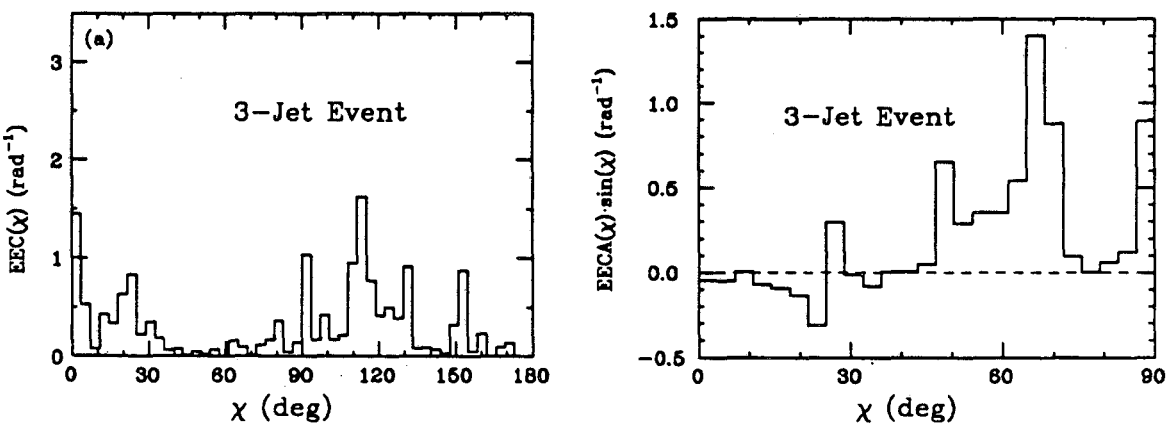

Figure 1.8 EEC and EECA for a three-jet event. *The EEC and EECA are shown for the three-jet event pictured in Fig. 1.5. The EECA has been weighted by* $\sin\chi$.

Of course, these examples represent the extremes of hadronic event shapes, but in a statistical sense these observations are true for all events—more and harder gluon radiation will produce a more asymmetric EEC. Furthermore, for angles $\chi \gtrsim$

30°, the EECA of the hadrons closely matches that of the underlying partons. To a good approximation, the EECA in this region is simply proportional to α_s, so it is well suited for measuring this constant.

Chapter 2. INTRODUCTION

The energy-energy correlation[9] (EEC) and its asymmetry (EECA) were introduced in 1978 as powerful estimators of the strong coupling constant, α_s. The EEC is an energy weighted angular correlation defined by

$$\mathrm{EEC}(\chi) = \frac{1}{N} \sum_{events}^{N} \sum_{i} \sum_{j} \frac{E_i E_j}{E_{cm}^2} \delta(\chi - \chi_{ij}) \tag{2.1}$$

where i and j run over all particles (charged and neutral) in the event, and χ_{ij} is the angle between particles i and j. The energy-energy correlation asymmetry (EECA) is conventionally defined as

$$\mathrm{EECA}(\chi) = \mathrm{EEC}(180^\circ - \chi) - \mathrm{EEC}(\chi). \tag{2.2}$$

Several experiments[10–16] have studied QCD processes by examining the EEC for hadronic events in e^+e^-annihilation. Simple $q\bar{q}$ events will produce back-to-back jets which will contribute to the EEC predominantly near $\chi = 0^\circ$ and $\chi = 180^\circ$. Events with hard gluon radiation, however, will populate the EEC at intermediate angles as well. In this way, the shape of the EEC is sensitive to α_s.

The advantage of the EEC over jet counting methods is that all hadronic events are used in the measurement and no special algorithms are required to distinguish jets or clusters. The EECA has the additional advantage that many of the effects of fragmentation and experimental error contribute symmetrically to the EEC, and thus cancel in the EECA. This leads to the expectation that an α_s measurement from the EECA should be much less fragmentation dependent than other measurements. In simulations, however, even the EECA shows sensitivity to the way the gluon is imbedded in the fragmentation scheme and how energy and momentum

are conserved in an event.[17–19] Nonetheless, the EECA remains a useful tool for studying hadronic events in e^+e^- annihilation.

We examine the EEC in e^+e^- collisions at a center-of-mass energy (E_{cm}) of 29 GeV. We use data from the original Mark II experiment at the PEP storage ring and from a PEP run of the Mark II after its recent SLC Upgrade. We compare our measured EEC and EECA with the predictions of second-order quantum chromodynamics (QCD) plus fragmentation models and determine α_s. We also compare our results with a leading log shower QCD model.

In 1982, the Mark II collaboration published a measurement of the EEC and EECA and made a first-order measurement of α_s.[20] Since that time the amount of data has increased four-fold and significant improvements have been made in QCD calculations and fragmentation models. The present results supersede the earlier ones.

Chapter 3. APPARATUS

The Mark II detector has operated in several different configurations. From Fall 1981 through Spring 1984, it accumulated 211 pb^{-1} in a configuration to which we refer by its experiment number, PEP-5. This detector is described in detail elsewhere.[21] Momenta of charged particles are measured with a sixteen-layer cylindrical drift chamber and a high-resolution vertex drift chamber immersed in a 2.3 kG axial magnetic field. The combined information provides a momentum resolution of $(\sigma_p/p)^2 = (0.025)^2 + (0.011p)^2$ (p in GeV/c).

In preparation for its impending run at SLC, the Mark II was extensively upgraded. The detector was operated at PEP in the upgraded configuration during 1985-1986, and about 30 pb^{-1} were logged. The general features of the Upgrade are described in the proposal.[22] Several components of the Upgrade contribute to the present analysis. A new 72-layer drift chamber[23] was installed together with a smaller trigger drift chamber.[24] This configuration, along with a new coil operating at a field of 4.5 kG, provides an improved momentum resolution for charged particles of $(\sigma_p/p)^2 = (0.014)^2 + (0.0026p)^2$. In addition, the acceptance for electromagnetic energy detection was increased by the addition of new end cap calorimeters[25] which cover polar angles θ such that $0.70 < |\cos\theta| < 0.95$. The end caps are constructed of 36 layers of lead and proportional tubes and provide an energy resolution of $\sigma_E/E = 0.2/\sqrt{E}$ (E in GeV) for photons and electrons.

The barrel calorimeter, common to both configurations, consists of eight modules of lead liquid argon shower counters and covers a range in polar angle of about $|\cos\theta| < 0.7$. Electromagnetic energy is measured in this region with a resolution of about $0.14/\sqrt{E}$.

Apart from the increased solid angle, the most important consequence of the upgrade is greatly improved two-track separation. The Upgrade drift chamber, with multiple hit readout capability and many more samples to aid in track identification,

has much higher efficiency for sorting out tracks in the core of a jet.

Chapter 4. TRACK AND EVENT SELECTION

All tracks are required to pass fairly tight quality and solid-angle cuts. This ensures that the momenta and angles are well measured and that the detection efficiency for these tracks is reliably described by the Monte Carlo detector simulation. The cuts used for both the PEP-5 and Upgrade detectors are identical except for the solid angle and sphericity axis cuts.

We accept only those charged and neutral tracks whose polar angles at their production points satisfy $|\cos\theta| \leq 0.68$ (0.85) for PEP-5 (Upgrade) data. This guarantees that only the highest efficiency region of the detector is used. For neutral particles with $|\cos\theta| \leq 0.7$, we require in addition that the detected shower be at least 3° from any of the eight cracks in ϕ between the barrel calorimeter modules.

Charged particles must have minimum transverse momenta with respect to the beam axis (p_{xy}) greater than 0.1 GeV/c. We cut on the distance of closest approach to the beam axis (r_{dca}) as follows:

$$r_{dca} \leq \begin{cases} 2mm, & p_{xy} > 1 \text{ GeV/c}; \\ \frac{2mm\ GeV/c}{p_{xy}}, & p_{xy} < 1 \text{ GeV/c}. \end{cases}$$

where the momentum dependence allows for multiple scattering of low momentum tracks. At the point of closest approach, we also require that separation from the event vertex along the beam (z) direction be less than 5 cm. Tracks with unphysically high measured momenta, $p > E_{beam}/c + 3\sigma_p$, are also removed. Since no particle identification is attempted, the pion mass is assigned to all charged tracks.

Accepted neutral tracks must deposit at least 0.5 GeV in the barrel or end cap calorimeters. In addition, each neutral shower must be separated by at least 30 cm from any charged track of momentum greater than the observed shower energy. This requirement helps to eliminate the fake photons that arise when charged hadrons interact in the coil.

Particles satisfying the above criteria are used in the selection of hadronic e^+e^- annihilation events. Such events must have at least five charged tracks, and the energies seen in charged particles (E_{ch}) must exceed 30% of E_{cm}. Each event must have a reconstructed primary vertex consistent with the mean beam interaction point (Δr <2 cm, Δz <10 cm). The sphericity axis[26] is determined from the charged particles, and we require that $|\cos\theta_{sph}| \leq 0.60$ (0.75) for PEP-5 (Upgrade) data, where θ_{sph} is the angle between the sphericity axis and the beam axis. The following cuts are made on momentum balance of charged tracks: $|\Sigma\vec{p}|/E_{ch} < 0.6$ and $|\Sigma p_z|/E_{ch} < 0.25$. These requirements help to eliminate highly-boosted events such as those which arise from initial-state radiation and the two-photon production process. Since any direct photon radiation can alter the EEC, we also discard events in which hard isolated photons are detected. Such photons are defined as those with $E_{shower} > 2.5$ GeV which are separated by more than 30 degrees from all charged tracks with $p_{ch} > 0.5$ GeV/c.

These event cuts are chosen to remove backgrounds from QED interactions, two-photon collisions, and beam gas collisions, and also to select well-measured events which contain ample information about the energy flow structure.

Finally, a special cut is used to remove remaining tau pairs. The charged particles are separated into two hemispheres by a plane perpendicular to the sphericity axis. For plausible tau topologies the invariant mass in each hemisphere is calculated. If this mass is less than 1.8 GeV/c^2 in both hemispheres, the event is rejected.

Only the highest quality data sets are used for this analysis. Notably, we omit PEP-5 runs in which the drift chamber was operated at reduced voltage. The samples which remain represent about 100 pb^{-1} of PEP-5 data and 24 pb^{-1} of Upgrade data. The cuts select 13,823 and 5,024 events, respectively. We estimate the contamination from two photon events to be about 1%, with negligible contributions from tau pairs and beam gas events.

Chapter 5. ENERGY-ENERGY CORRELATION MEASUREMENT

The EEC is accumulated from all accepted charged and neutral particles according to the formula

$$\mathrm{EEC}(\chi_k) = \frac{1}{N} \sum_{events}^{N} \sum_{i} \sum_{j} \frac{E_i E_j}{E_{vis}^2} \left(\frac{1}{\Delta\chi} \int_{\chi_k - \Delta\chi/2}^{\chi_k + \Delta\chi/2} \delta(\chi - \chi_{ij}) d\chi \right), \qquad (5.1)$$

for 50 discrete bins in χ ($\Delta\chi = 3.6°$).[27] Note that the detected charged plus neutral energy (E_{vis}) is used to normalize each weight rather than E_{cm} so that undetected particles have less influence on the EEC.

The uncorrected EEC and EECA distributions for both detector configurations are shown in Fig. 5.1. The self-correlation contribution is responsible for the spike which appears in the lowest bin in Fig. 5.1(a). The large peaks near 0° and 180° show the predominance of two-jet events. The width of these peaks can be attributed to both fragmentation effects and the emission of soft and collinear gluons. At intermediate angles ($30° < \chi < 150°$), however, QCD predicts that major contributions come from three- and four-parton events produced by hard gluon radiation. The large difference between the two EEC measurements near 90° is expected from the larger solid angle coverage of the Upgrade.

Before we draw conclusions from our data, we must take account of detector effects. This is accomplished by applying a simple multiplicative correction factor to the data:

$$\mathrm{EECA}_{cor}(\chi) = C(\chi) \cdot \mathrm{EECA}_{data}(\chi). \qquad (5.2)$$

The EEC itself is corrected separately in the same manner. The correction factors, C, are used to compensate for the effects of initial state radiation, detector acceptance, track and event selection bias, detection efficiency, and resolution.

The corrections are determined with a Monte Carlo simulation, and in principle they can depend on the parameters that go into the simulation, including the value

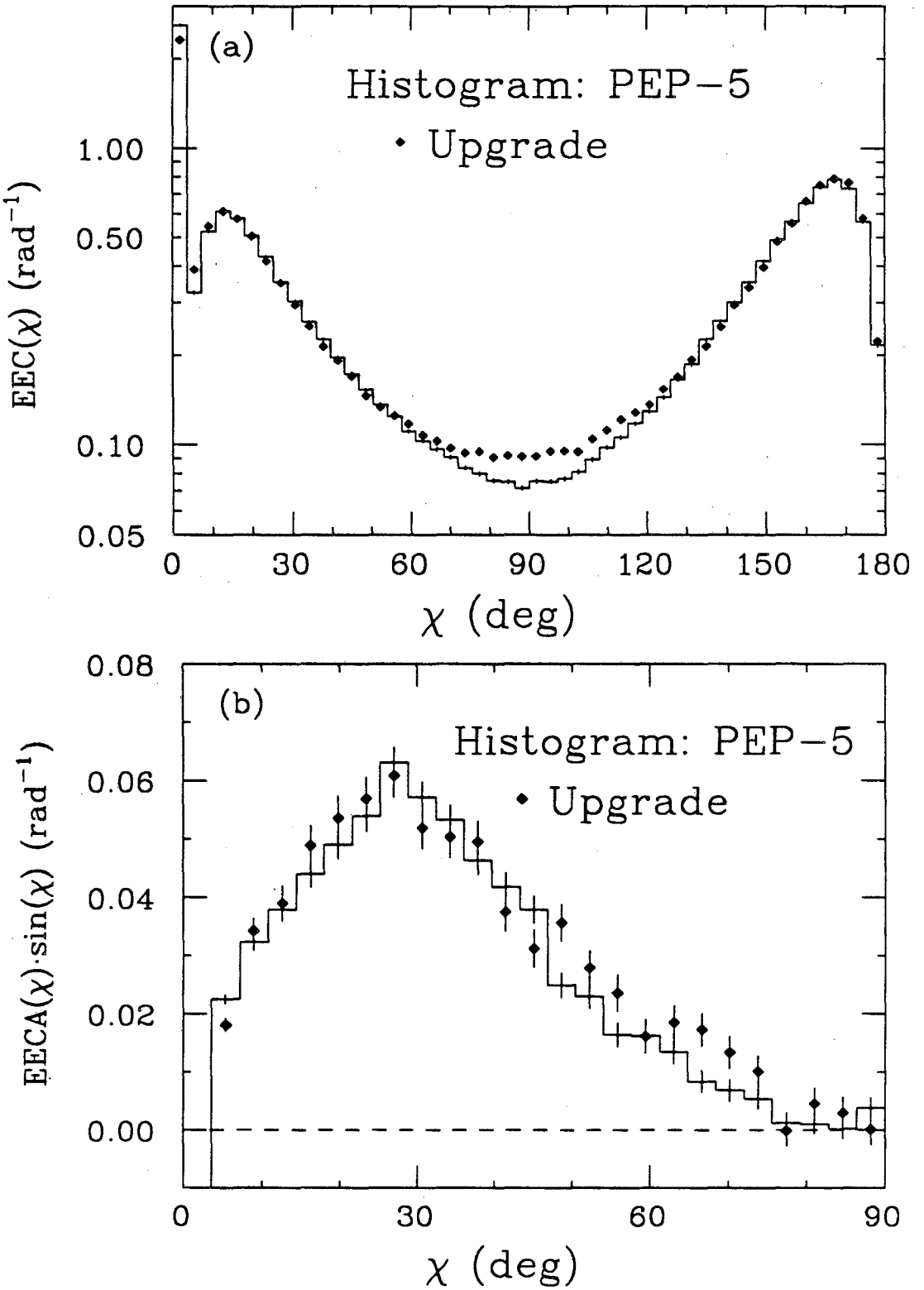

Figure 5.1 Raw EECs (a) and EECAs (b). *The data are from two detector configurations described in the text. No corrections have been made for acceptance, resolution, or efficiency.*

of α_s.[28] Ideally, we would completely reevaluate the factors $C(\chi)$ for each value of α_s and each model that we consider. The computer time required is prohibitive, however, if we employ a complete detector simulation in each instance. Consequently, the correction factor C is taken to be the product C_1C_2 of two separate factors whose precise definitions will be given below, following a more detailed description of our Monte Carlo simulation. Qualitatively, the factor C_2 takes account of initial state radiation and the gross geometry of the detector. It is sensitive to simulation model parameters and the value of α_s. On the other hand, the factor C_1, which provides the relation between full detector simulation and the gross geometric corrections included in C_2, is close to unity and relatively insensitive to model assumptions. Thus the time-consuming calculation of C_1 need be done for only one set of model parameters, while the determination of C_2, which has to be repeated for many parameter and α_s choices, is relatively modest in its computer time requirements.

The Monte Carlo simulation is used in three modes: the event generator alone (GEN), the generator with gross geometric acceptance corrections and initial state radiation (AC), and a detailed full detector simulation (FS). The event generator produces a list of four-vectors for the final state particles (including neutrinos) and is completely independent of the detector configuration. It includes the effects of QCD, fragmentation, and decays of short-lived particles. When the FS is included, the trajectory of each of the particles produced by the event generator is traced and the interactions with the active and passive material in the detector are simulated in detail. A simulated raw data image is produced which is subsequently processed by the same event reconstruction program as is used for the real data. This simulation has been extensively studied and tuned to reproduce reliably the observed detector performance.

The AC accounts for the detector effects in a simpler but more approximate manner. It uses the particle four-vectors directly from the event generator, but accepts only the detectable, stable particles ($e^{\pm}, \mu^{\pm}, \pi^{\pm}, K^{\pm}, p, \bar{p}, \gamma$) that are pointed into the acceptance region of the detector. Momenta and energies are not smeared,

the detection efficiency is assumed to be 100% within the specified solid angle, and the pion mass is assigned to all charged particles. Track and event selection cuts, based on quantities determined from these accepted particles, are applied subsequently. The effects of initial state radiation are included as well.[29] For many studies, the AC would be grossly inadequate, but for the EEC it incorporates the most important experimental effects (solid angle, radiative corrections, and event selection bias) without requiring the time-consuming full simulation.

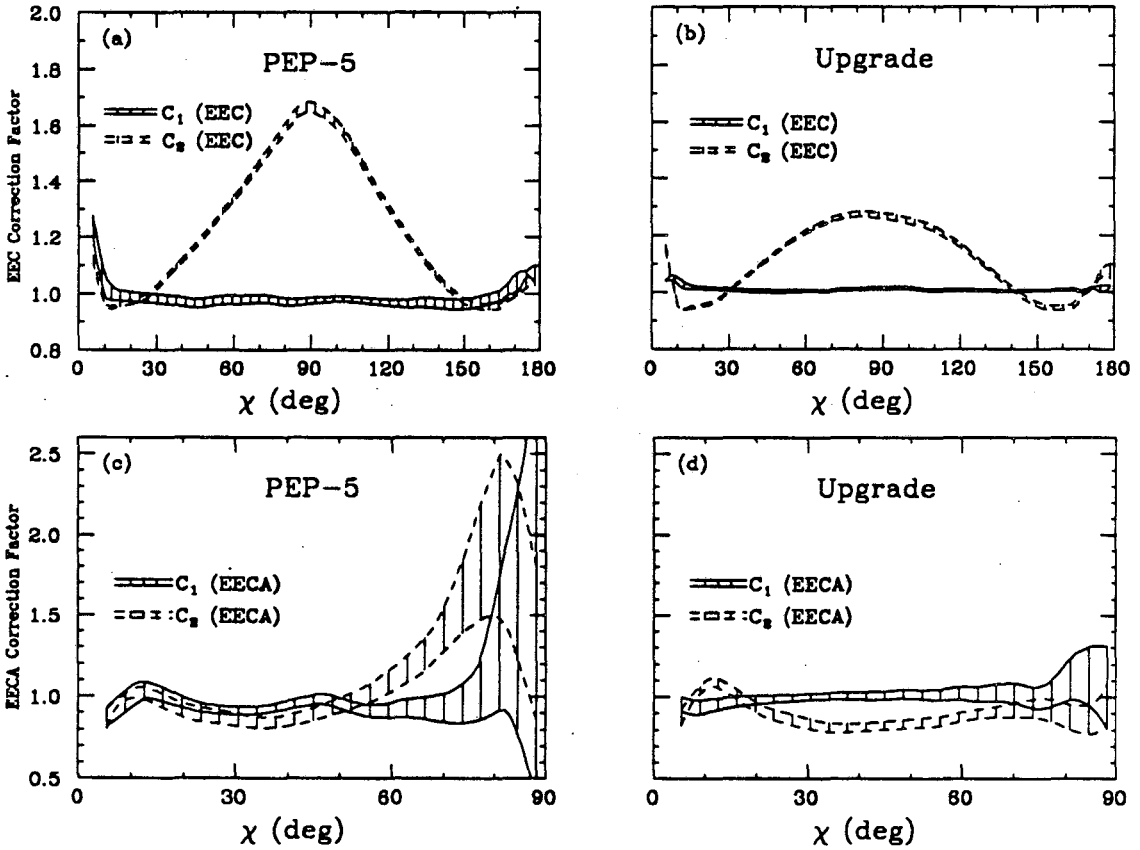

Figure 5.2 Correction factors for the EEC and EECA. *The two factors C_1 and C_2 (described in the text) are shown separately with solid and dashed curves respectively. The hashed regions show the errors assigned to these factors.*

We define the correction factors C_1 and C_2 for the EECA as follows:

$$C_1(\chi) = \mathrm{EECA}_{AC}(\chi, \alpha_s^0)/\mathrm{EECA}_{FS}(\chi, \alpha_s^0) \tag{5.3}$$

$$C_2(\chi, \alpha_s) = \mathrm{EECA}_{GEN}(\chi, \alpha_s)/\mathrm{EECA}_{AC}(\chi, \alpha_s), \tag{5.4}$$

and similarly for the EEC. The correction factors C_1 are determined from large hadronic Monte Carlo samples which are carried through the full detector simulation. For these samples, there is reasonably good agreement with the data for most observables, including the EEC and EECA. Figure 5.2 shows the calculated C_1 and C_2 for the two detector configurations. Bands are used to indicate the systematic uncertainties on these factors. The bin to bin fluctuations are smoothed out in the central region of the EEC corrections ($14.4° \leq \chi \leq 165.6°$) by convolution with a Gaussian. For the asymmetry correction, Gaussian smoothing is used for $\chi \geq 10.8°$. The large corrections to the EECA near 90° are of little consequence because the asymmetry itself is vanishing in this region. Note that, aside from this, the corrections made with C_1 are $\lesssim$10% within the regions used for α_s studies.

In order to estimate the systematic errors on C_1, we separate the Monte Carlo events into three sub-samples according to the number of charged particles generated: low multiplicity ($n_{ch} \leq 10$), medium multiplicity ($n_{ch} = 12, 14$), and high multiplicity ($n_{ch} \geq 16$). The combined sample approximately reproduces the measured average multiplicity of 12.9 ± 0.6,[30] and this decomposition divides the sample into roughly equal thirds. The quantity C_1 is calculated separately for the high and low multiplicity sub-samples, and the deviation between the two is used as an estimate of the systematic error. This should be considered a realistic estimate of the systematic error because the largest contribution to deviations from unity in C_1 is the loss of detected tracks in crowded environments. The contributions to the systematic error from Monte Carlo statistics are also included where they are appreciable. The widths of the bands in Fig. 5.2 indicate the sizes of the total systematic errors.

In addition, C_1 is checked for model dependence. Figure 5.3 shows a comparison between two determinations of C_1 for the PEP-5 detector. One is obtained from a sample of Lund string[31] Monte Carlo and is shown with the errors discussed above.

The other is determined from a comparable sample of independent fragmentation[32] Monte Carlo. The two calculations of C_1 are consistent within errors. Similar checks for the Upgrade detector give very good agreement between calculations of C_1 with string fragmentation and shower models.

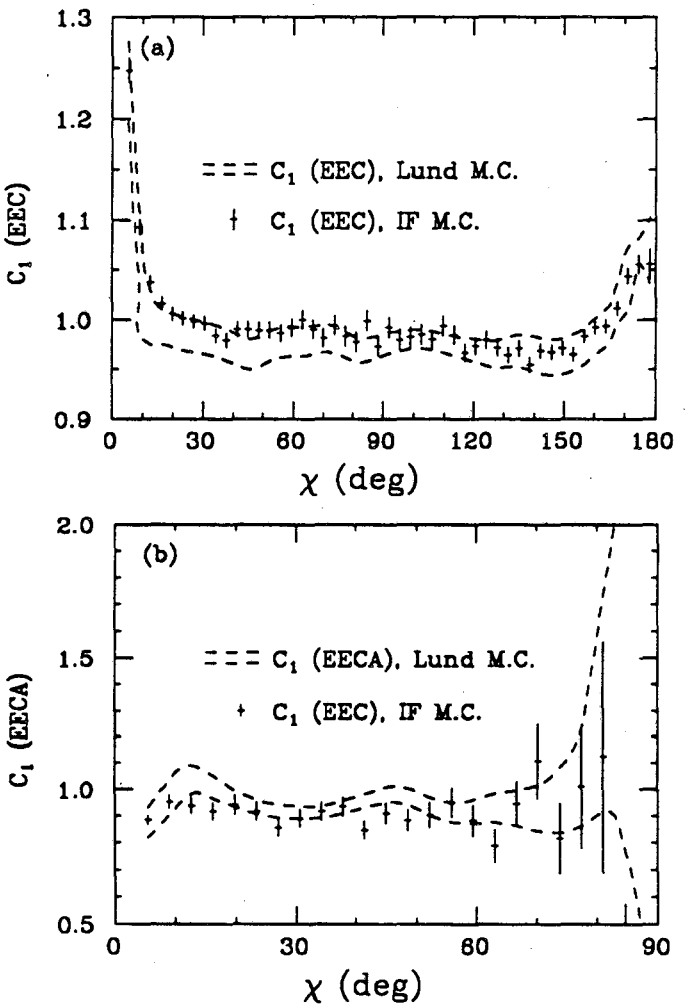

Figure 5.3 Comparison of PEP-5 C_1 from Lund and IF samples. *The dashed band shows C_1 as determined from the Lund sample. The width of the band indicates the size of the systematic errors assigned to C_1. The points show C_1 from the independent fragmentation sample, and the error bars are from the IF Monte Carlo statistics.*

For the PEP-5 detector, the tracking efficiency has been studied in detail. In hadronic events, the Monte Carlo has been found to overestimate the true single track efficiency by $1.5\% \pm 3.0\%$.[33] The effects of overestimating the efficiency are evaluated by analyzing a large block of data (not used elsewhere in our analysis)

for which the drift chamber was operated at reduced voltage, resulting in a 10% degradation in efficiency. From a comparison between this and the higher quality data, we conclude that the efficiency uncertainties can be neglected in the EEC and EECA measurements.

For the Upgrade data, we study the effect of the two-track separation on the efficiency. The two-hit resolution is altered in the detector Monte Carlo to be slightly worse than what is observed in the data, and this is found to have a negligible effect on C_1.

We make an explicit check for any bias remaining from a dependence of C_1 upon α_s. We calculate C_1 for Monte Carlo samples in which the two-, three-, and four-parton components are reweighted to simulate values of α_s from .11 to .20. C_1(EECA) changes by less than 1% for $\chi > 30°$ over this entire range of α_s for both PEP-5 and Upgrade configurations.

For the purpose of determining the best detector-independent measures of the EEC and EECA, the corrections C_2 are calculated from a large AC Monte Carlo sample generated with a value of α_s=0.158 with the Lund String Monte Carlo[31] and the Gottschalk and Shatz matrix element.[6] This value of α_s corresponds to our measurement described in the next section. To establish the errors on C_2 due to α_s uncertainty and model dependence, we recalculate C_2 with four different Monte Carlo samples: Lund String with α_s=0.141, Lund String with α_s=0.173, Hoyer Independent Fragmentation[34] with α_s=0.105, and Lund Shower[31] with Λ_{LLA}=400 MeV. The two string Monte Carlo samples represent roughly the two-sigma limits (statistical and systematic) of our measured value of α_s. The comparison of the four calculations yields an estimated uncertainty in C_2 for each bin in χ, and this is used to assign the systematic errors which appear in Fig. 5.2.

Our fully corrected EEC and EECA distributions with separate statistical and systematic errors are given in Table 5.1 and Table 5.2. Note that when summing bins in χ, the statistical errors may be added in quadrature, but the systematic errors are strongly correlated. To allow simple comparisons with models and other experiments, we give here the integrals over the conventional intervals:[36]

$$\int_{57.6^\circ}^{122.4^\circ} \mathrm{EEC}(\chi)d\chi = \begin{cases} .1486 \pm .0005 \pm .0018 \pm .0014, & \text{PEP-5;} \\ .1458 \pm .0007 \pm .0006 \pm .0010, & \text{Upgrade,} \end{cases}$$

$$\int_{28.8^\circ}^{90^\circ} \mathrm{EECA}(\chi)d\chi = \begin{cases} .0297 \pm .0008 \pm .0010 \pm .0016, & \text{PEP-5;} \\ .0306 \pm .0010 \pm .0006 \pm .0010, & \text{Upgrade,} \end{cases}$$

where the first error is statistical and the second and third are the systematic errors which result from the uncertainties on C_1 and C_2, respectively.

The fully corrected data are shown with combined errors in Fig. 5.4. The agreement between the two detector configurations is quite good. In Fig. 5.5, we compare our EECA directly to those of MAC,[14] JADE,[12] CELLO,[10] and PLUTO[16] who correct their data in a similar fashion. Note that only the MAC results were obtained at the same energy.

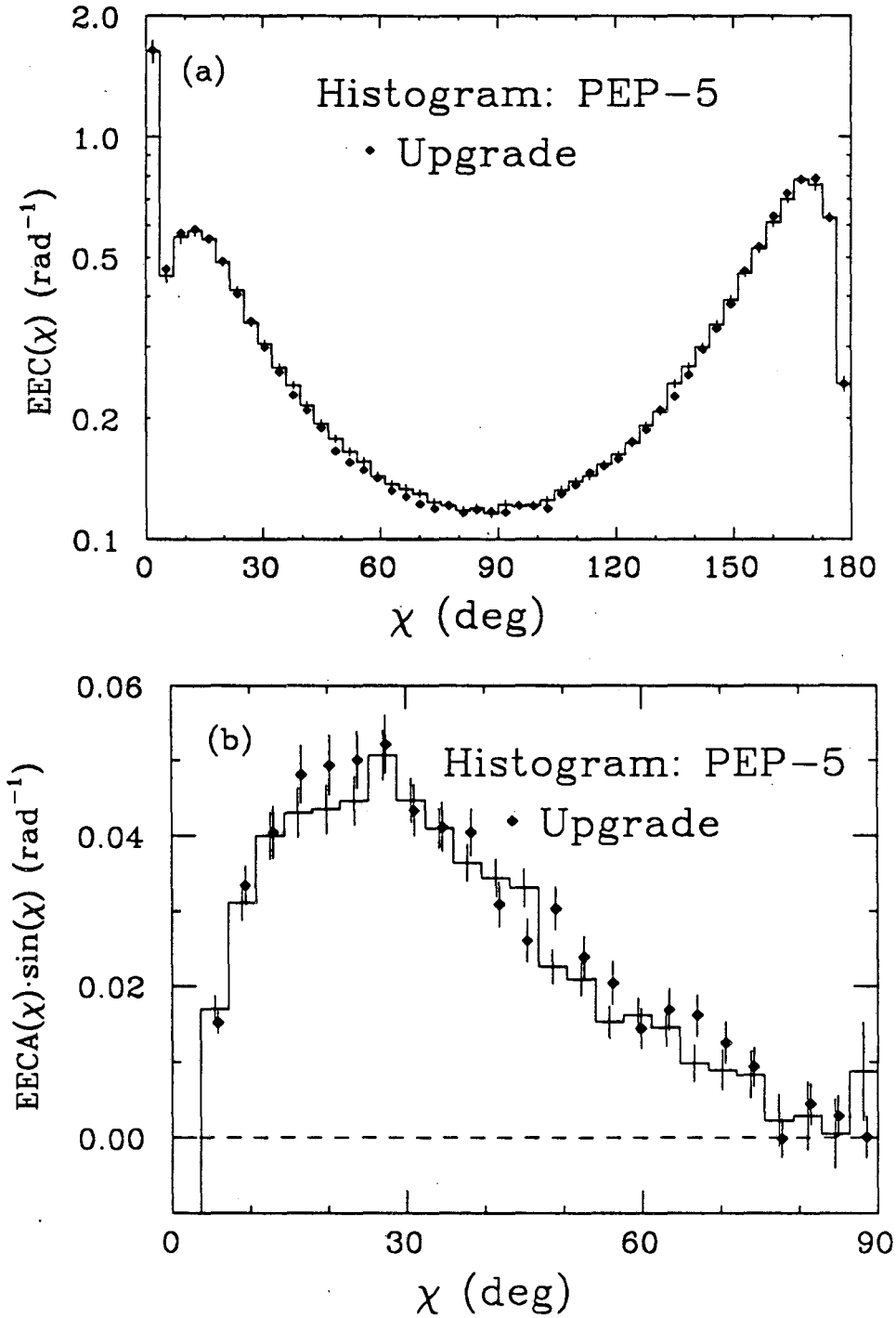

Figure 5.4 Fully corrected data. *The fully corrected EEC and EECA are shown separately for the PEP-5 and Upgrade detectors. The errors shown are the sum in quadrature of the statistical and systematic errors.*

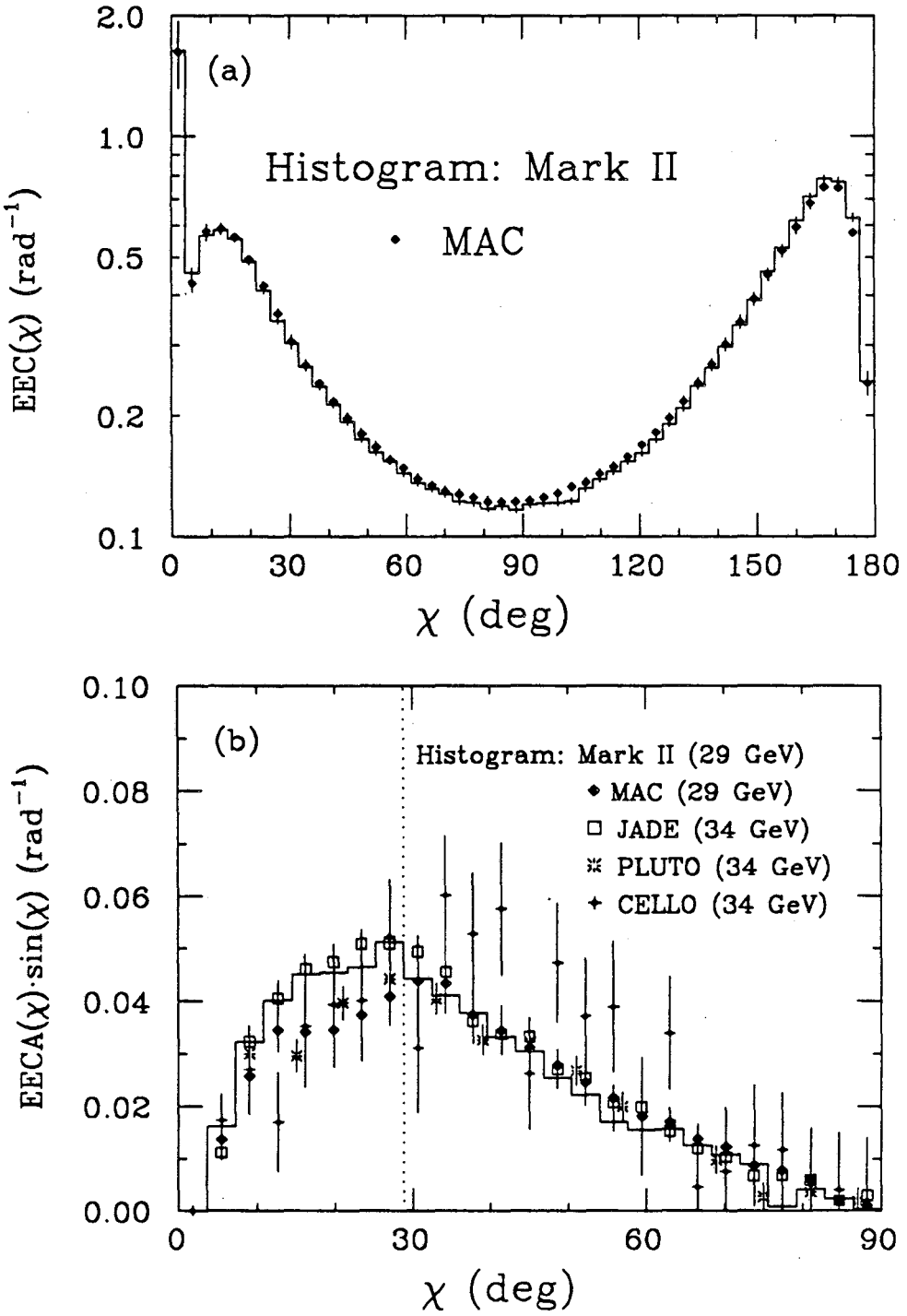

Figure 5.5 Comparison to other experiments. *The fully corrected EEC and EECA (PEP-5 and Upgrade combined) are compared with fully corrected data from other e^+e^- experiments. The Mark II and MAC results are at $\sqrt{s}$=29 GeV while the others are at $\sqrt{s}$=34 GeV. The region of the EECA above the dotted line in (b) is used to measure α_s.*

Table 5.1 **Fully corrected EEC, $(rad^{-1}) \times 10^3$.** *Statistical errors are followed by systematic errors.*

χ (degrees)	PEP-5 EEC	Upgrade EEC	χ (degrees)	PEP-5 EEC	Upgrade EEC
0.0 - 3.6	1633±9±103	1645±15±37	90.0 - 93.6	122±2±2	117±3±1
3.6 - 7.2	451±6±15	468±8±3	93.6 - 97.2	121±2±2	121±3±1
7.2 - 10.8	563±6±20	576±8±7	97.2 - 100.8	122±2±2	121±3±1
10.8 - 14.4	583±5±16	589±7±7	100.8 - 104.4	125±2±2	119±2±1
14.4 - 18.0	556±5±11	557±7±4	104.4 - 108.0	133±2±2	130±3±1
18.0 - 21.6	486±4±9	489±6±3	108.0 - 111.6	140±2±2	137±3±1
21.6 - 25.2	415±4±8	405±5±3	111.6 - 115.2	144±2±2	147±3±1
25.2 - 28.8	345±3±6	347±5±2	115.2 - 118.8	154±2±2	152±3±1
28.8 - 32.4	306±3±6	299±4±2	118.8 - 122.4	163±2±2	159±3±1
32.4 - 36.0	268±3±5	260±4±2	122.4 - 126.0	174±2±3	175±3±1
36.0 - 39.6	241±3±4	228±3±2	126.0 - 129.6	192±2±3	188±3±1
39.6 - 43.2	215±2±4	209±3±1	129.6 - 133.2	208±2±4	210±4±1
43.2 - 46.8	194±2±3	190±3±1	133.2 - 136.8	243±3±5	226±4±2
46.8 - 50.4	178±2±3	167±3±1	136.8 - 140.4	268±3±5	256±4±2
50.4 - 54.0	165±2±3	156±3±1	140.4 - 144.0	300±3±6	296±5±2
54.0 - 57.6	156±2±3	149±3±1	144.0 - 147.6	340±4±7	333±5±3
57.6 - 61.2	144±2±2	142±3±1	147.6 - 151.2	393±4±8	384±6±3
61.2 - 64.8	137±2±2	132±3±1	151.2 - 154.8	457±4±10	463±7±4
64.8 - 68.4	134±2±2	128±2±1	154.8 - 158.4	526±5±11	531±7±5
68.4 - 72.0	130±2±2	123±2±1	158.4 - 162.0	611±5±13	633±8±6
72.0 - 75.6	124±2±2	119±2±1	162.0 - 165.6	700±6±15	723±9±7
75.6 - 79.2	121±2±2	121±3±1	165.6 - 169.2	781±7±16	783±11±4
79.2 - 82.8	118±2±2	116±2±1	169.2 - 172.8	760±8±24	790±12±5
82.8 - 86.4	119±2±2	118±2±1	172.8 - 176.4	627±8±14	626±11±10
86.4 - 90.0	116±2±2	117±2±1	176.4 - 180.0	243±5±9	243±7±6

Table 5.2 **Fully corrected EECA,** $(rad^{-1}) \times 10^3$. *Statistical errors are followed by systematic errors.*

χ (degrees)	PEP-5 EECA	Upgrade EECA
0.0 - 3.6	-1389± 9± 97	-1399± 15± 31
3.6 - 7.2	180± 6± 17	161± 10± 11
7.2 - 10.8	199± 9± 14	214± 13± 11
10.8 - 14.4	183± 10± 12	186± 14± 8
14.4 - 18.0	154± 8± 9	173± 12± 7
18.0 - 21.6	128± 6± 7	146± 10± 6
21.6 - 25.2	112± 5± 6	126± 8± 5
25.2 - 28.8	112± 5± 6	115± 7± 5
28.8 - 32.4	88± 4± 4	85± 6± 3
32.4 - 36.0	73± 3± 3	73± 5± 3
36.0 - 39.6	59± 3± 3	66± 5± 3
39.6 - 43.2	52± 3± 3	47± 4± 2
43.2 - 46.8	47± 3± 2	37± 4± 1
46.8 - 50.4	30± 3± 2	40± 4± 2
50.4 - 54.0	26± 2± 2	30± 3± 1
54.0 - 57.6	18± 2± 1	25± 3± 1
57.6 - 61.2	19± 2± 1	17± 3± 1
61.2 - 64.8	16± 2± 1	19± 3± 1
64.8 - 68.4	11± 2± 1	18± 3± 1
68.4 - 72.0	10± 3± 1	13± 3± 1
72.0 - 75.6	9± 3± 2	10± 3± 1
75.6 - 79.2	2± 3± 1	0± 3± 0
79.2 - 82.8	3± 4± 1	5± 3± 1
82.8 - 86.4	1± 5± 0	3± 3± 1
86.4 - 90.0	9± 4± 8	0± 3± 0

Chapter 6. α_s DETERMINATION

To measure α_s, we compare our data with the $O(\alpha_s{}^2)$ perturbative QCD predictions for $e^+e^- \rightarrow$ quarks and gluons. We use the recent dressed matrix element calculation of Gottschalk and Shatz.[6] Previous measurements used either the ERT[3] or FKSS/GKS[4] matrix element calculations. The differences among these are discussed in detail in Ref. 7, and the new calculation incorporates significant terms that are neglected in the GKS matrix element. The calculation assumes massless partons, and quark masses are inserted *a posteriori*. The individual two-, three-, and four-parton cross sections are separated by employing a y_{min} cutoff of 0.015, where $y_{ij} = (p_i + p_j)^2/s$ is the scaled invariant mass of a pair of partons. We verify that the predicted EECA is stable at small values of this infrared cutoff, as shown in Fig. 6.1.

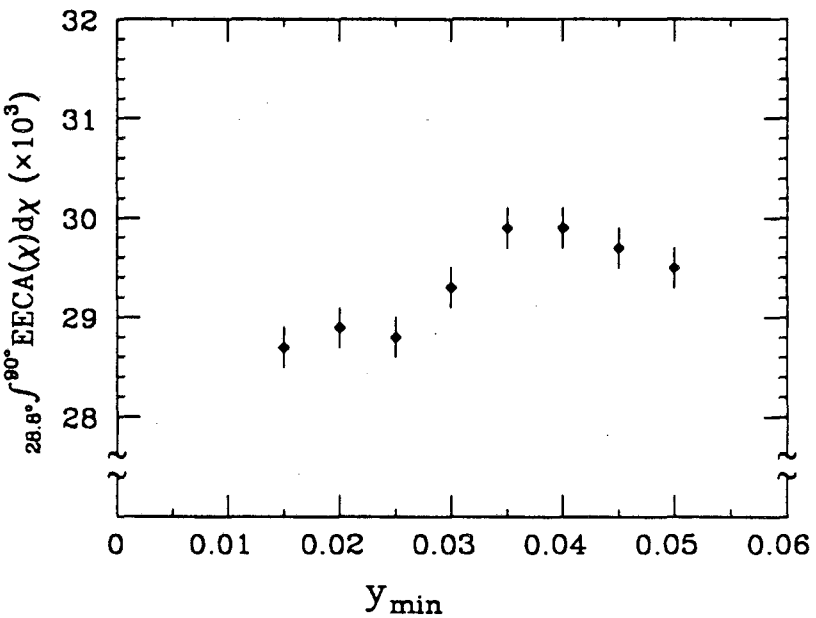

Figure 6.1 Cutoff stability of the EECA. *The integrated asymmetry is shown from Monte Carlo samples generated with the Gottschalk and Schatz matrix element and Lund string fragmentation for several values of the infrared cutoff parameter* y_{min}.

To account for fragmentation effects, we use the Lund string model with the Lund symmetric fragmentation function. This model is quite successful in describing the general features of our data,[35] and, in particular, it favorably reproduces the distribution of particles in three-jet events.[37,38] We comment on the effects of fragmentation models more fully in the next section. The parameters of the model have been initially chosen to describe the global features of our data, including distributions of multiplicity, momentum, and sphericity.[35,39]

To determine α_s, we compare our data with high-statistics samples of Monte Carlo events generated with five different values of α_s. Only the detailed detector corrections represented by the factor $C_1(\chi)$ are applied to the data, and the radiative and gross acceptance effects are included in the Monte Carlo simulations to which the data are compared. Thus the effects of α_s on the properties of the generated events and the geometric acceptance are properly included.

Our best estimates of α_s are obtained from a χ^2 comparison between the data and Monte Carlo EECA distributions as just described. We limit the sensitivity to fragmentation effects in $q\bar{q}$ events by utilizing the EECA information only for a limited region in χ, namely $\chi \geq 28.8°$ (17 bins). Only statistical errors are considered in the χ^2 calculations. The results are shown in Fig. 6.2. Parabolas are fitted to the χ^2 points, and from the positions of the minima and the curvatures we obtain the values and errors of α_s:

$$\alpha_s = \begin{cases} 0.155 \pm .004, & \text{PEP-5;} \\ 0.159 \pm .004, & \text{Upgrade;} \end{cases}$$

where the errors are statistical only. These values each correspond to $\chi^2 \approx 20$ for 16 degrees of freedom.

The statistical error on the Upgrade measurement is comparable to that from the PEP-5 measurement in spite of the smaller number of events. This is a consequence of the larger solid angle and higher efficiency of the Upgrade detector, since the statistical precision of the EECA measurement improves not only with the number of events but also with the number of particles detected in each event.

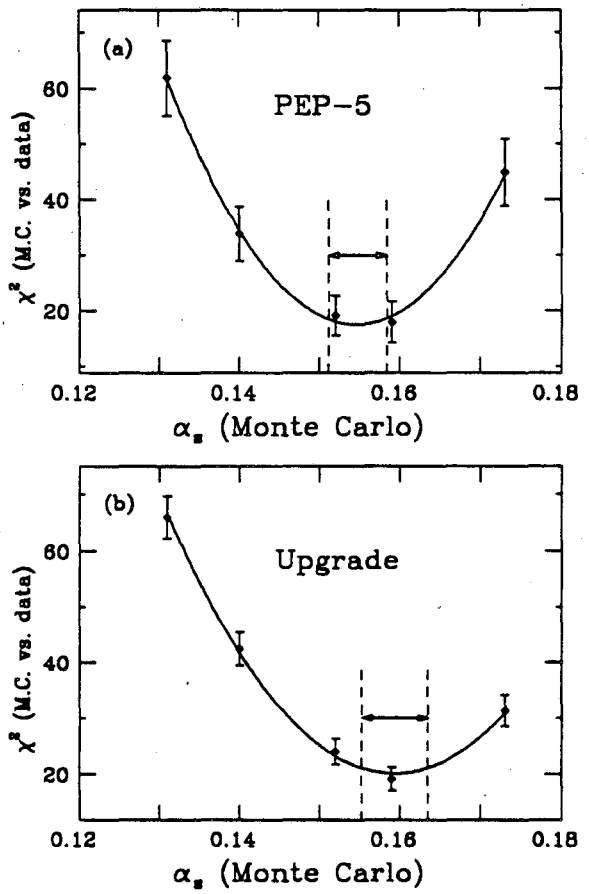

Figure 6.2 χ^2 **comparison between data and Monte Carlo.** *The points represent a χ^2 (for 17 data points) calculated from comparing the EECA with Monte Carlo data generated at several values of α_s. The errors represent the expected variation of this quantity with the Monte Carlo statistics. The curves are parabolas fitted through the points, and the locations of the minima indicate the best values of α_s. The vertical lines show the one-sigma statistical errors on α_s.*

The details of the fragmentation introduce additional systematic uncertainties into the α_s determination. Hadronization in the string model is governed largely by the parameters σ_q, A and B. The momenta of hadrons along the string direction is obtained from the symmetric Lund fragmentation function[40]

$$f(z) = \frac{1}{z}(1-z)^A \exp -(Bm_\perp^2/z), \tag{6.1}$$

where $m_\perp^2 = (m^2+p_\perp^2)$ and z is the fraction of $(E+p_{||})$ acquired by the hadron. The transverse momenta are distributed according to a gaussian of width σ_q. The fragmentation parameters A and B are strongly correlated, and therefore B is left fixed

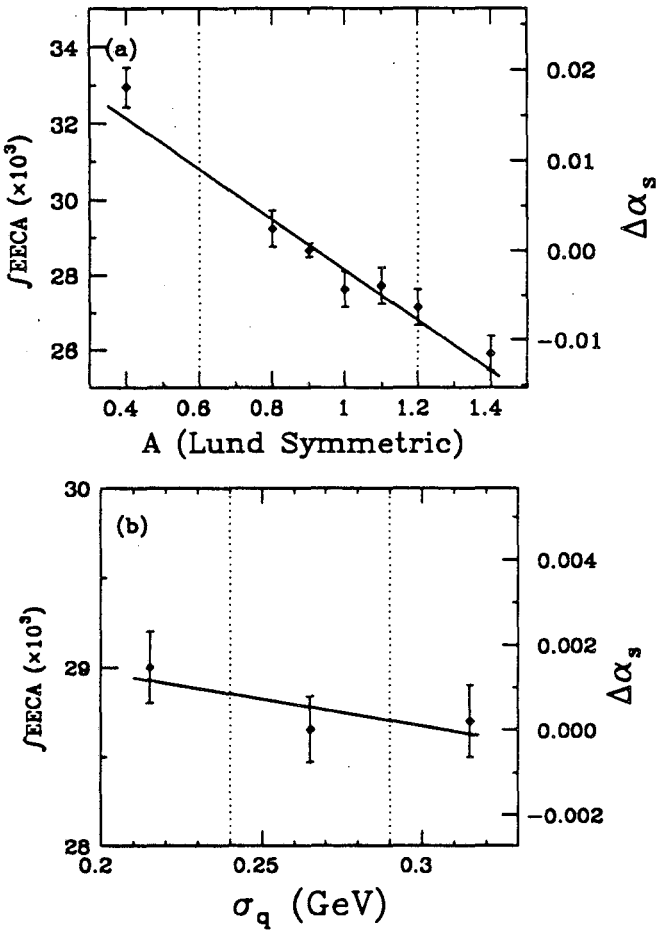

Figure 6.3 Sensitivity of the EECA to model parameters. *We show the integrated EECA from Monte Carlo samples at the generator level. The EECA is integrated over the range* $28.8° < \chi < 90°$ *and plotted vs. (a) the parameter A in the Lund symmetric fragmentation function, and (b)* σ_q*. The one-sigma limits of these parameters are indicated with the dotted lines. The right-hand scales show the changes in the measured value of* α_s *which result from different choices of the parameter values.*

at 0.7 GeV^{-2} while A is varied over a range that agrees with the observed charged particle multiplicity, namely $.6 \leq A \leq 1.2$. A small correlation exists between the multiplicity and the input value of α_s which is accounted for in the systematic errors. If both A and B are varied so as to maintain a constant multiplicity, the variations in the EEC are negligible. The range of σ_q is confined to be between .240 GeV and .290 GeV in order to give reasonable agreement with the distribution of particle momenta normal to the sphericity plane ($p_\perp^{out}$).[35] The detailed shape of the EECA for $\chi > 30°$ is insensitive to small changes in these parameters, and therefore

the integrated EECA is used to investigate the systematic errors. Figure 6.3 shows the changes introduced by varying A and σ_q.

We have also tried using Peterson[41] fragmentation functions for heavy quarks. The measured spectra of D^* mesons provide strong limits on the fragmentation function parameter ϵ_c,[42] and the fractional uncertainty on α_s introduced by the allowed variations is less than 1%.

The contributions from tau pair and two photon backgrounds are estimated with Monte Carlo simulations. They are found to have negligible effects on the α_s measurement.

Table 6.1 Systematic errors on α_s measurement.

Source	PEP-5 EECA	Upgrade EECA
Data correction	3.3%	1.8%
σ_q	1.3%	1.1%
Frag. param and mult.	4.6%	4.6%

It has been shown recently that the second order QCD matrix elements underestimate the ratio of four-jet to three-jet events.[43] The deficiency in the four-jet rate presumably results from the lack of higher order contributions. Thus we can roughly estimate the size of higher order effects by artificially increasing the hard four-parton cross section accordingly. We carry out this procedure by doubling the four-parton rate[44] in the Monte Carlo and then determining α_s. This results in a decrease of .005 in the measured value of α_s. We do not include this effect in our systematic errors, however, because we are quoting α_s at $O({\alpha_s}^2)$.

The sources and their estimated contribution to the uncertainty in α_s are summarized in Table 6.1. The data correction errors are derived from the uncertainties on C_1. The total systematic errors (combined in quadrature) are .009 (.008) for PEP-5 (Upgrade). We have not included the effects of different fragmentation models in the systematic errors; these are discussed separately in the following section.

We quote errors for the Lund model alone because it is the only $O(\alpha_s{}^2)$ model that adequately describes our data.

The results from the two configurations are now combined to give $\alpha_s(29\ \text{GeV})=0.158 \pm 0.003 \pm 0.008$. This α_s value is used to generate Monte Carlo events which are compared with the data in Fig. 6.4 and Fig. 6.5. The agreement is very good for both the EEC and the EECA. The data in these figures are fully corrected and are identical to the Mark II data shown in Fig. 5.5 except that the self-correlation contributions are removed from the lowest bin for clarity.

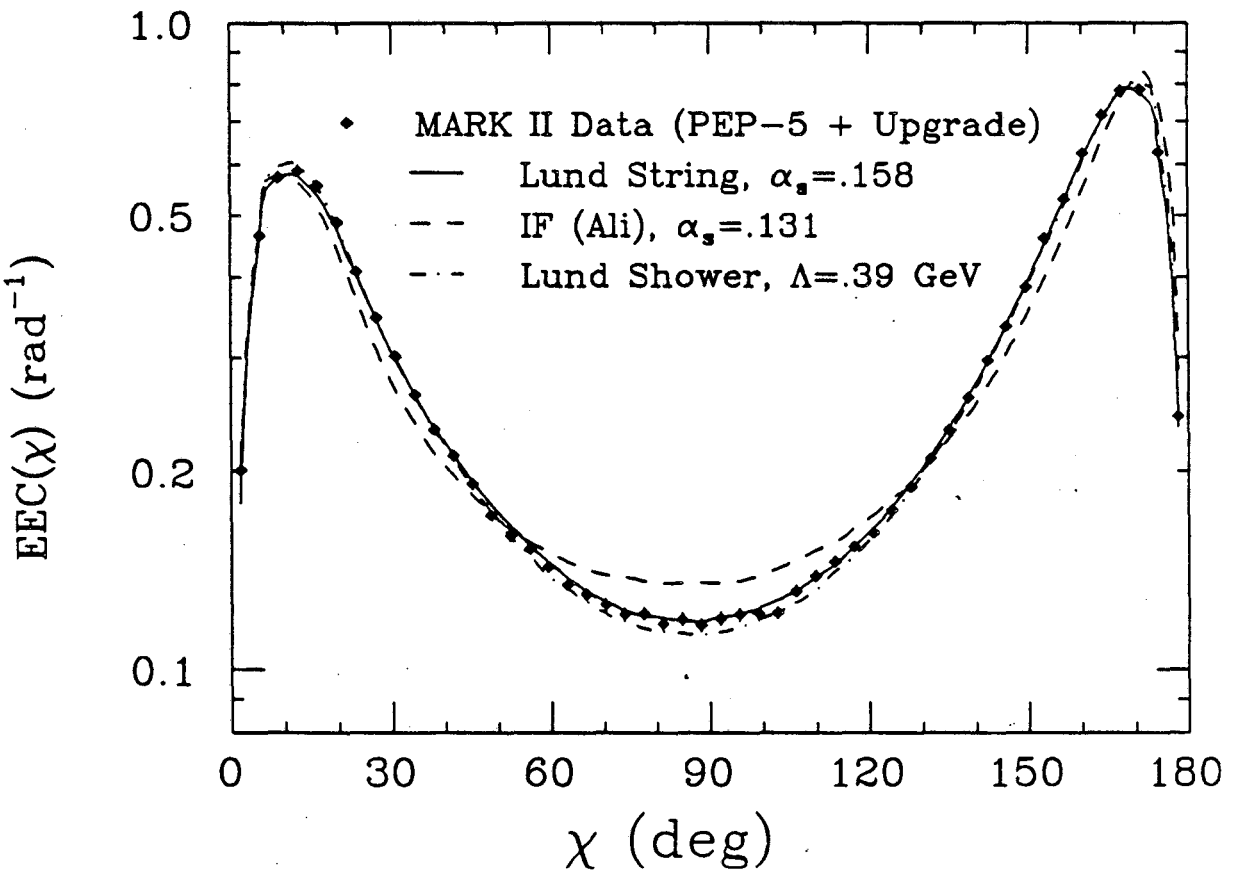

Figure 6.4 Comparisons of EEC with Monte Carlo. *The predictions of several models are compared to the corrected EEC. The self-correlation contributions are removed from the lowest bin to make the figure more clear. The values of α_s or Λ_{LLA} are chosen from fits of the Monte Carlos to the EECA. The curve for IF (Hoyer) α_s=.102 is not drawn because it coincides with the Ali curve.*

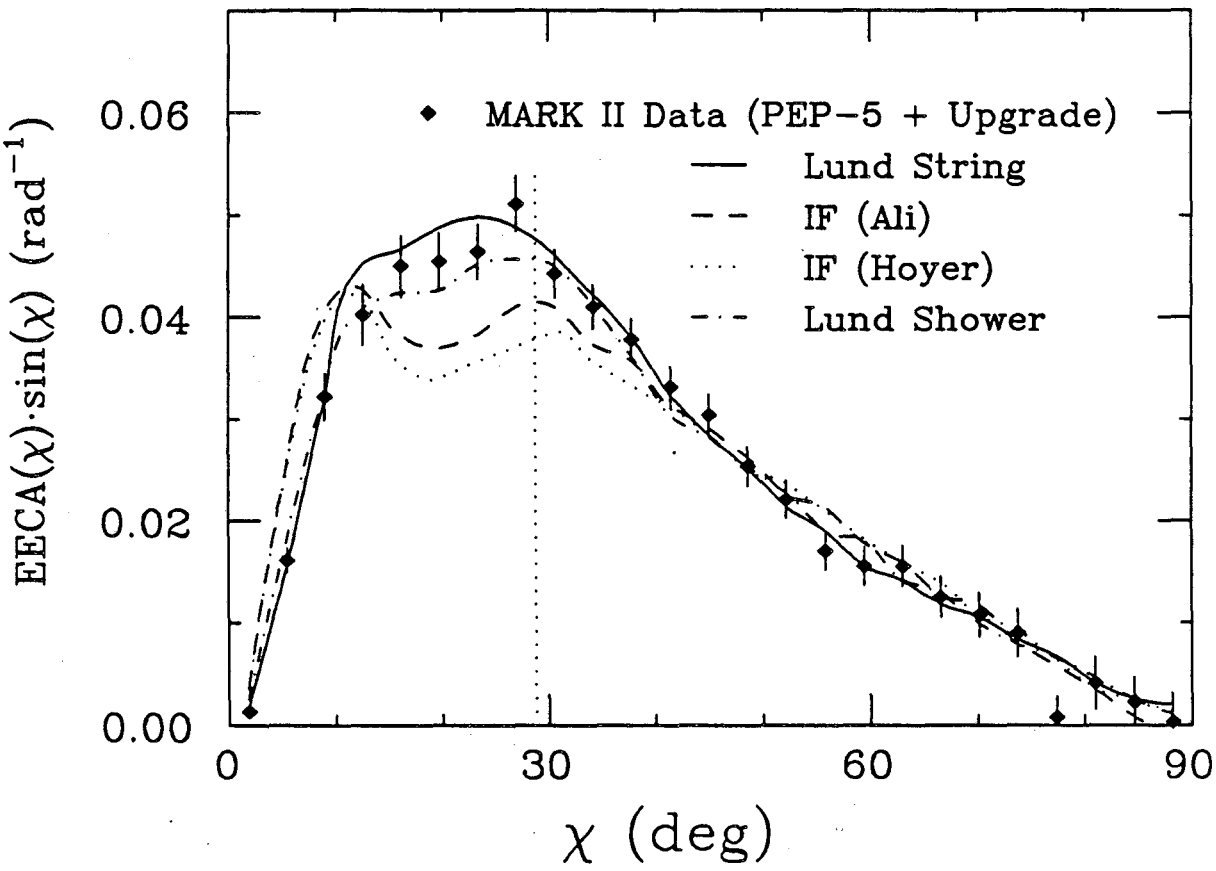

Figure 6.5 Comparisons of EECA with Monte Carlo. *The results of the best fits to the EECA are shown for four different Monte Carlo generators: α_s=0.158 for Lund String, α_s=0.131 for Ali, α_s=0.102 for Hoyer and Λ_{LLA}=390 MeV for Lund Shower. The fits are performed over the region above the dotted line.*

The QCD scale parameter Λ is related to α_s by

$$\alpha_s = \frac{2\pi}{\frac{(33-2N_f)}{6}\ln\left(\frac{Q^2}{\Lambda^2}\right) + \frac{(153-19N_f)}{(33-2N_f)}\ln\left(\ln\left(\frac{Q^2}{\Lambda^2}\right)\right)}, \tag{6.2}$$

in the $\overline{MS}$ renormalization scheme,[1] where N_f is the number of flavors open. At Q=29 GeV with N_f=5, our α_s value corresponds to $\Lambda_{\overline{MS}}$=330 ± 40 ± 70 MeV.

Our result is compared with other EECA measurements of α_s in Fig. 6.6. The present measurement is, as expected, in better agreement with the ERT values than with those obtained from the FKSS/GKS matrix element.[7] For the sake of comparison, we repeat our analysis using the GKS matrix element, and we obtain $\alpha_s(29\ \text{GeV})=0.174\pm0.004\pm0.009$. Both results appear in the figure, where they are scaled to Q=34 GeV according to Eqn. 6.2.

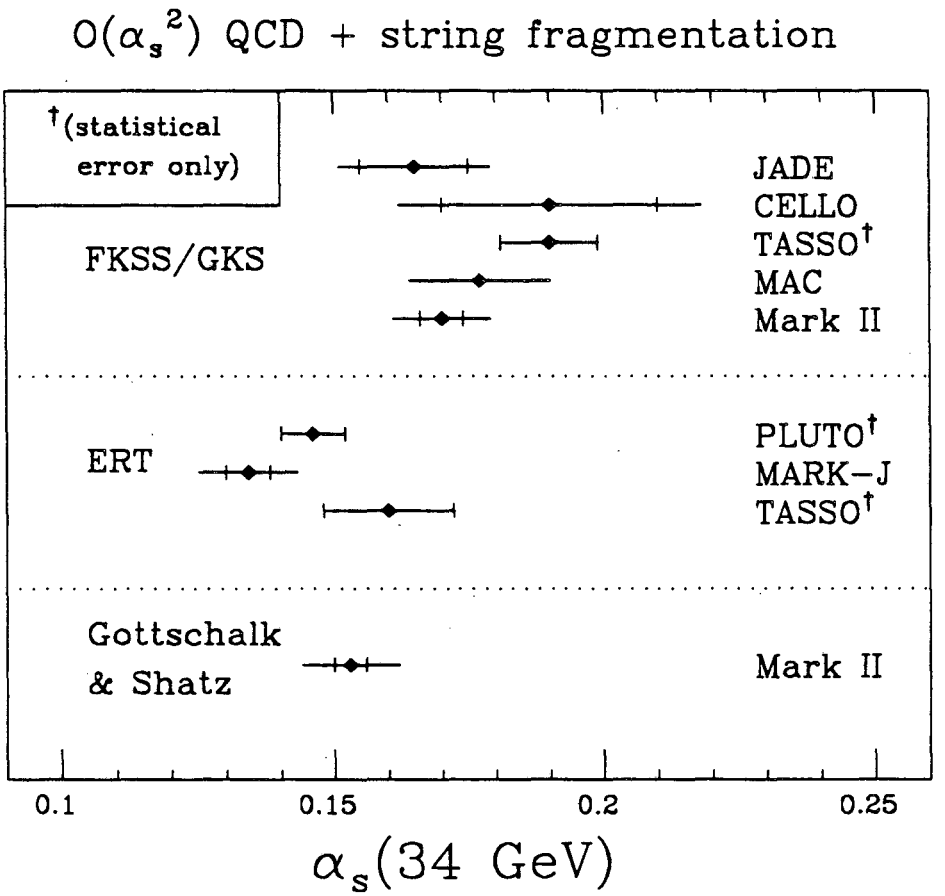

Figure 6.6 Comparison of α_s measurements. *Our value of α_s is compared to those from similar experiments, taken from Ref. 45. The horizontal bars represent the statistical and systematic errors (where available) added in quadrature. The vertical bars indicate the size of the statistical errors alone. All values were obtained by comparing the EECA with an $O(\alpha_s^2)$ matrix element plus Lund string fragmentation. The results are grouped according to the matrix element calculations used, which are indicated at the left. All measurements are at $\sqrt{s}$=34 GeV, except for Mark II and MAC which are rescaled from 29 GeV to 34 GeV according to Eqn. 6.2 ($\Delta\alpha_s \approx$-0.005). Where two points appear for the same experiment, they are not statistically independent.*

Chapter 7. MODEL COMPARISONS

Several alternatives exist to the string fragmentation model which enjoy varying degrees of success in describing hadronic events at these energies. We examine some of these briefly in regard to the EEC and EECA.

Independent fragmentation (IF) models are the most common alternative to string fragmentation. Since IF models do not automatically conserve momentum and energy, a particular method must be chosen to accomplish this, and this appears to be the dominant source of uncertainty in measuring α_s. The two cases we examine here are the Ali scheme,[46] where jet angles are adjusted and energies are preserved, and the Hoyer scheme,[34] where the opposite prescription is imposed. A fit to the EECA using the Ali scheme gives an α_s value of 0.131 ± 0.003 (statistical). Concurrent agreement with the EEC, however, cannot be achieved with any reasonable value of σ_q. The Hoyer scheme represents an even more extreme departure from the string model. It yields $\alpha_s = 0.102 \pm 0.003$ (statistical) and similar disagreement with the EEC. The results of a best fits to the EECA are shown in Fig. 6.4 and Fig. 6.5. In each case, the model parameters A, B, and σ_q are tuned to give agreement with the average multiplicity and $p_\perp^{out}$ from the data. These results concur with other experiments[11–16] which found that IF models tend to give lower values of α_s.

Finally, we compare our data with a leading-log QCD shower Monte Carlo. As an example, we show the EEC from the Lund shower model, Version 6.3.[31] This model includes a matrix-element weighting of the first branching, and coherence effects are included by angular ordering of subsequent parton emission. As for the string model, the parameters have been adjusted to reproduce a variety of distributions.[35] The agreement of this model with the EEC and EECA data is quite good, as shown in Fig. 6.4 and Fig. 6.5.

In the shower model, the amount of gluon emission is determined by the QCD

scale parameter Λ_{LLA}. We determine this parameter from the EECA just as we measure α_s. We find $\Lambda_{LLA} = 390 \pm 30$ MeV (statistical). The definitions of $\Lambda_{\overline{MS}}$ and Λ_{LLA} are sufficiently different that the agreement should be viewed as fortuitous.

The best agreement between the global features of the data and the shower model is obtained at a very low shower cutoff value (Q_0=1 GeV).[35] The EECA, however, shows little sensitivity to this cutoff for $Q_0 \lesssim 4$ GeV, as shown in Fig. 7.1. In contrast to the results of PLUTO,[16] who showed that an earlier shower model was unable to describe their EECA, this good agreement reflects recent improvements in leading-log models.

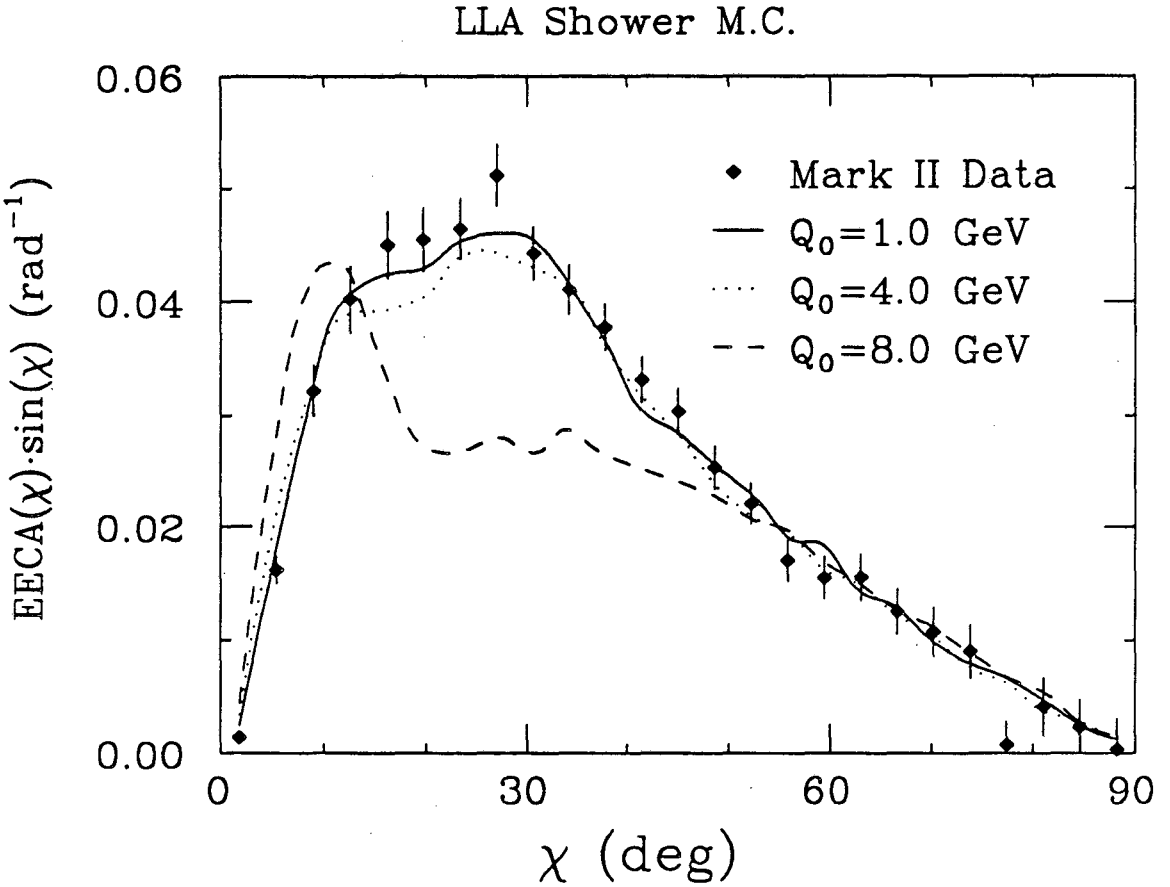

Figure 7.1 Cutoff sensitivity in the shower model. *The EECA predicted by the Lund Shower Monte Carlo is shown for three different values of the shower cut off mass, Q_0. The fragmentation parameters A, B, and σ_q are adjusted for each Q_0 value to maintain a constant multiplicity and $p_\perp^{out}$ spectrum, but Λ_{LLA} is fixed at 400 MeV.*

Chapter 8. SUMMARY

We have studied the energy-energy correlation in e^+e^- annihilation into hadrons at 29 GeV. We have used data from the Mark II detector both before and after its upgrade for the SLC, and we find good agreement between the two data sets. We also compare our data to the published results of other experiments. We find reasonable agreement with the EEC and EECA distribution from MAC, which has also operated at 29 GeV. The agreement is best in the perturbative region of the EECA ($\chi \gtrsim 30°$). PETRA experiments at 34 GeV also compare well in this region.

We determine α_s from our EECA measurement. The results from the PEP-5 and Upgrade data agree well, and give a combined value of $\alpha_s = 0.158 \pm 0.003 \pm 0.008$ when we use the matrix element calculation of Gottschalk and Shatz and string fragmentation. This result is in reasonable agreement with similar measurements made with the ERT matrix elements, and is about 10% lower than FKSS/GKS determinations. Independent fragmentation models yield considerably lower values of α_s (0.11-0.14).

Both the EECA and EEC are described well by the Lund string model, but cannot be simultaneously fit with independent fragmentation models. The recent Lund leading-log shower model also describes both distributions well with a QCD scale parameter of $\Lambda_{LLA} = 390 \pm 30$ MeV.

Acknowledgements

The authors are grateful to S. Bethke for many useful discussions and for providing computer code for the Gottschalk and Shatz matrix element. This work was supported in part by Department of Energy contracts DE-AC03-81ER40050 (CIT), DE-AA03-76SF00010 (UCSC), DE-AC02-86ER40253 (Colorado), DE-AC02-76ER03064 (Harvard), DE-AC03-83ER40103 (Hawaii), DE-AC02-84ER40125 (In-

diana), DE-AC03-76SF00098 (LBL), DE-AC02-84ER40125 (Michigan), and DE-AC03-76SF00515 (SLAC), and by the National Science Foundation (Johns Hopkins).

Appendix A. APPARATUS (II)

Here we expand on the brief description of the apparatus given in Chapter 3.

A.1 THE PEP STORAGE RING

All of the data contributing to this work were obtained at the PEP (Positron Electron Project) e^+e^- storage ring at SLAC. This 1.5 mile ring operates at an energy of 14.5 GeV in each beam. The electrons and positrons are orbited in three bunches each, providing beam crossings at each of six interaction points every 2.4 μsec. Typical luminosities are about $1\text{-}2\cdot10^{31} cm^{-2} sec^{-1}$.

A.2 THE MARK II DETECTOR

A.2.1 History

The Mark II detector is a general purpose magnetic detector for e^+e^- collisions. The design is based on that of the SLAC-LBL Magnetic Detector (Mark I) at the SPEAR storage ring, and the Mark II itself was originally installed at SPEAR as well. There it studied e^+e^- collisions at center of mass energies from 3 GeV to 7 GeV in the period 1977-79.

In 1979 the Mark II moved to PEP and began taking data there in Fall 1981. Shortly thereafter, two major changes were made in the detector: A precision vertex drift chamber was installed, and the magnetic field was reduced to half strength (2.3 kG) because of a short in the coil. The Mark II continued to operate in this configuration through Spring 1984, by which time it had accumulated about 205 pb^{-1} of data with the vertex chamber.

In 1983, the Mark II was selected as the first detector for the planned SLAC Linear Collider (SLC). Since the SLC is designed to provide e^+e^- collisions at the energy of the Z^0 ($\approx$93 GeV), the Mark II collaboration began a program of detector upgrades to meet the demands of this new energy regime. Some important considerations were:

- good momentum measurement up to 50 GeV/c
- efficient track reconstruction in dense jet environments, and
- large solid angle coverage.

A thorough discussion of the correspondence between the physics motivations and the hardware upgrades can be found in the Upgrade proposal.[47]

In the Fall and Winter of 1985-86, the upgraded Mark II (Upgrade) was operated at PEP. This run provided a thorough check-out of the new components and of the newly integrated detector system. In addition, the Upgrade detector accumulated a reasonably substantial set of data ($\approx$30 pb^{-1}) with which to study physics at 29 GeV. These data also provide a benchmark with which to compare the forthcoming SLC data.

A.2.2 General Description

The geometry of the Mark II is approximately described by a series of coaxial cylinders as seen in the isometric views in Fig. A.1 and Fig. A.2. The elements are nested one within another, and we describe them in order of progressively larger radius.

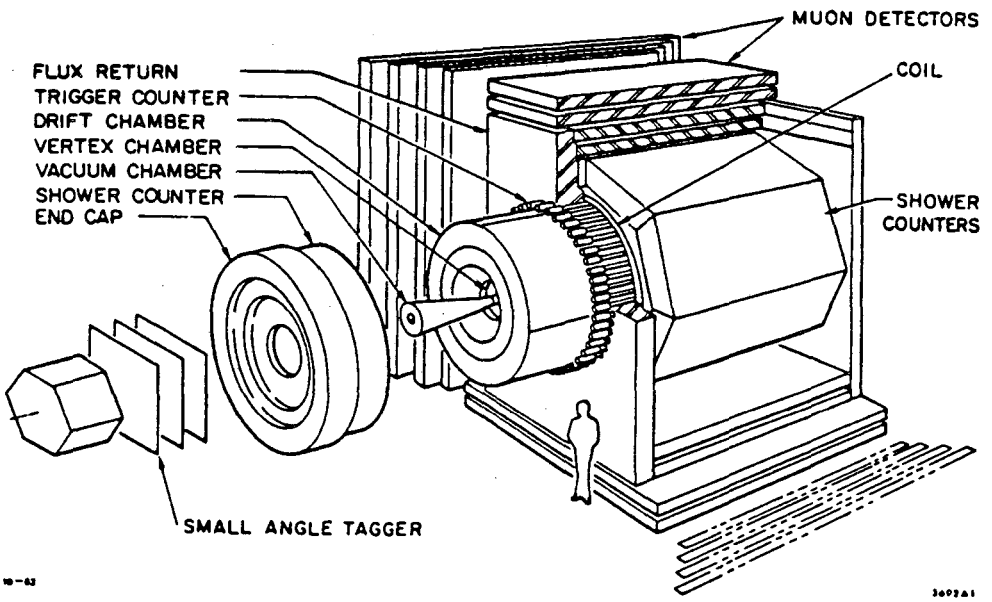

Figure A.1 The Mark II detector at PEP (PEP-5).

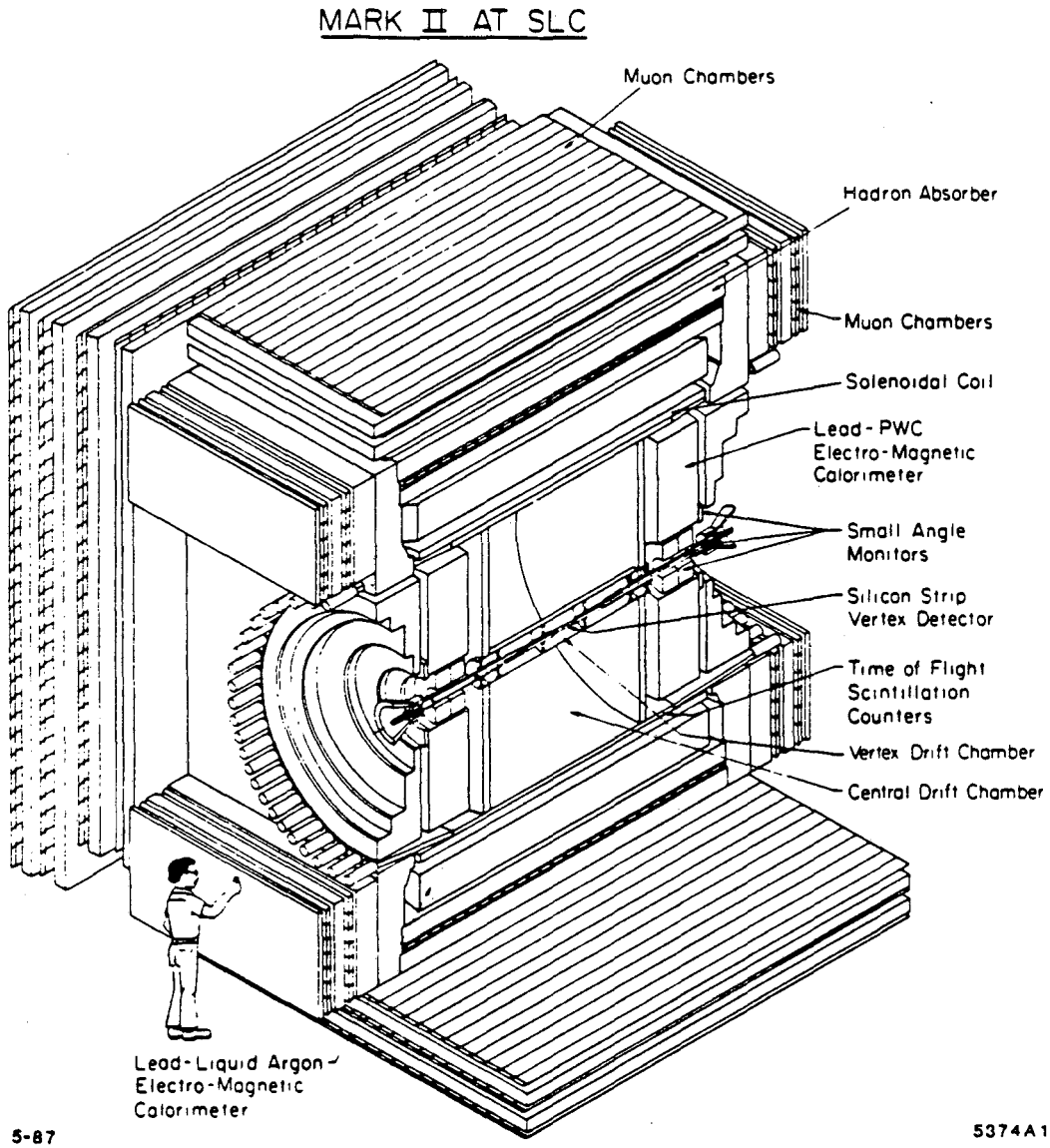

Figure A.2 The Mark II detector for SLC (Upgrade). *This figure depicts several components which were not present when the Upgrade operated at PEP, namely the silicon strip vertex detector, the vertex drift chamber, the small angle monitors, and the forward muon system. At PEP, the position of the vertex drift chamber was occupied by the trigger chamber.*

Immediately surrounding the beam pipe is a precision tracking chamber known as the vertex chamber (trigger chamber) in the PEP-5 (Upgrade) detector. This is followed by a large (1.5 meter radius) drift chamber. Together these chambers provide the charged particle tracking for the Mark II.

A cylindrical array of scintillators surrounds the drift chamber. These counters provide time-of-flight (TOF) information that can aid in particle identification for low-momentum hadrons, and are also used in triggering and cosmic ray rejection.

A solenoid encloses the TOF system, drift chamber, and inner tracking chamber. The field is oriented parallel to the beam axis with a strength of 2.3 kG (4.5 kG) in the PEP-5 (Upgrade) configuration.

The electromagnetic calorimetry system lies just outside of the coil. In the barrel region ($|\cos\theta| \lesssim 0.7$) showers are detected in liquid argon calorimeter modules. For the Upgrade detector, the end cap region ($0.70 \lesssim |\cos\theta| \lesssim 0.95$) is covered by lead/proportional tube calorimeters. In the PEP-5 detector, shower counters consisting of 2.3 radiation lengths of lead and two layers of proportional tubes partially cover this region. The PEP-5 end caps, however, are not used in this analysis.

The outermost part of the Mark II is devoted to muon detection. Four layers of proportional tubes are sandwiched between layers of steel absorber. The innermost layer of steel forms the return yolk for the solenoid.

Finally, in the very forward regions of the PEP-5 detector, a small angle tagger (SAT) is used to identify electrons produced at small angles from the beam axis. It consists of planes of drift chambers followed by lead/scintillator shower counters.

For the purpose of this analysis, the charged tracking system is of central importance. It will be discussed in more detail in the following section. The calorimetry systems also make important contributions to the measurement, so they are also described more fully.

A.2.3 Charged Particle Tracking

In the PEP-5 detector, charged particles are tracked with the combined information from a vertex drift chamber and a main drift chamber. With a 2.3 kG magnetic field, this system provides a momentum resolution of $(\sigma_p/p)^2 = (0.025)^2 + (0.011p)^2$ (p in GeV/c).

The vertex chamber had four thin bands of sense wires at a radius of 11.5 cm and three more at 31 cm, and the azimuthal spacing between sense wires was about

1 cm. The chamber was filled with a mixture of 50% argon and 50% ethane at atmospheric pressure.

The main drift chamber had sixteen concentric bands of sense wires equally spaced in radii from 41 cm to 145 cm. The drift cells, which are depicted in Fig. A.3, each contained one sense wire and had widths of 1.8 cm in the inner six layers and 3.6 cm in the outer 10 layers. A gas mixture of 50% argon and 50% ethane was also used in the main drift chamber. The position resolution was about 220 μm in each cell.

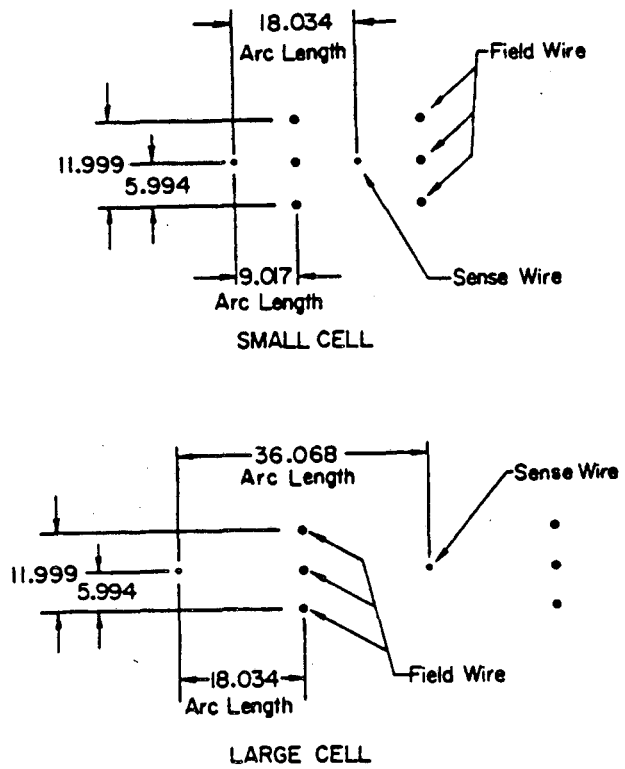

Figure A.3 Cell design for the PEP-5 drift chamber. *Dimensions are given in millimeters.*

The main drift chamber was replaced in the Upgrade. Since the new drift chamber extends down to a smaller radius than the old and thus cannot accommodate the PEP-5 vertex chamber, a special trigger chamber was constructed to operate inside of it for the PEP running. This system was immersed in a 4.5 kG

axial field, and achieved a momentum resolution of $(\sigma_p/p)^2 = (0.014)^2 + (0.0026p)^2$.

The trigger chamber is composed of 552 proportional cells, each consisting of a 4.0 mm diameter mylar straw with a 20 μm sense wire in the center. The cells are arranged in six layers with radii between 9.5 cm and 14.8 cm. During the operation at PEP, a gas mixture of 50% argon 50% ethane was circulated through each cell, and the position resolution was measured to be about 90 μm.

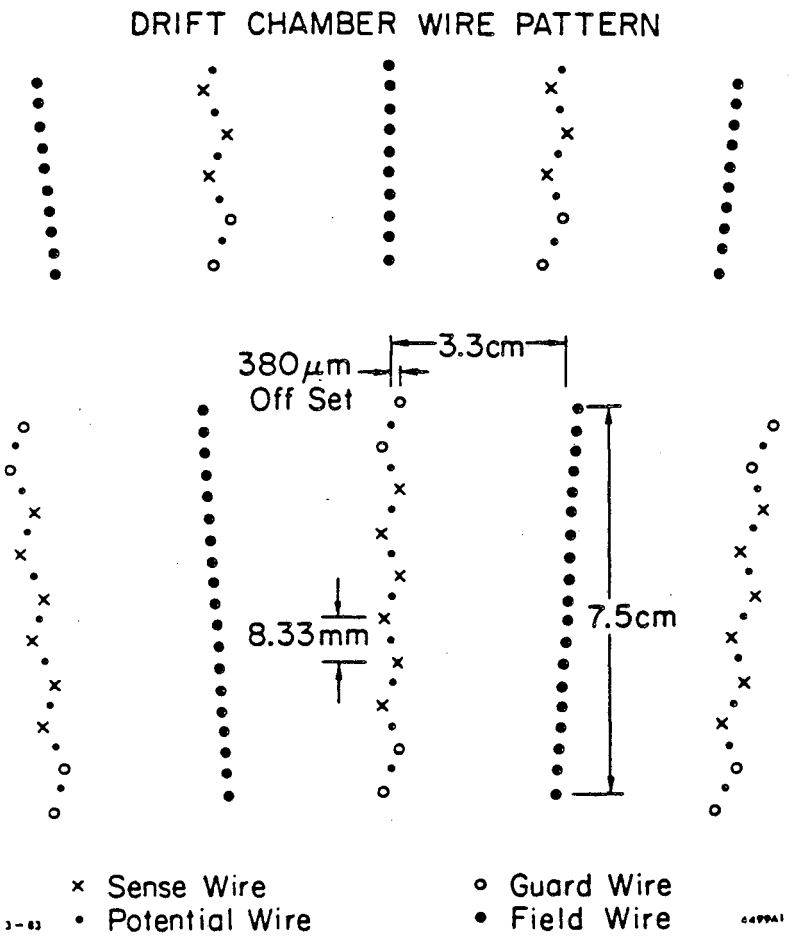

Figure A.4 Upgrade Drift Chamber cell design. *The chamber contains 972 such cells.*

The design of the new drift chamber differs considerably from that of the old. The 72 layers of sense wires are divided into 12 "superlayers" of six sense wire layers each. The superlayers are subdivided azimuthally into multi-sense-wire cells, shown in Fig. A.4, which are shortened versions of the jet-chamber configuration.[48]

Although these cells are actually larger than those of the old drift chamber, they achieve far better two-track separation because the readout electronics are able to distinguish and record multiple hits on each wire. This improved two-track resolution (4mm - 6mm) and the natural pattern recognition afforded by the jet-cell design yield a much higher tracking efficiency in dense jets, as seen in Fig. A.5.

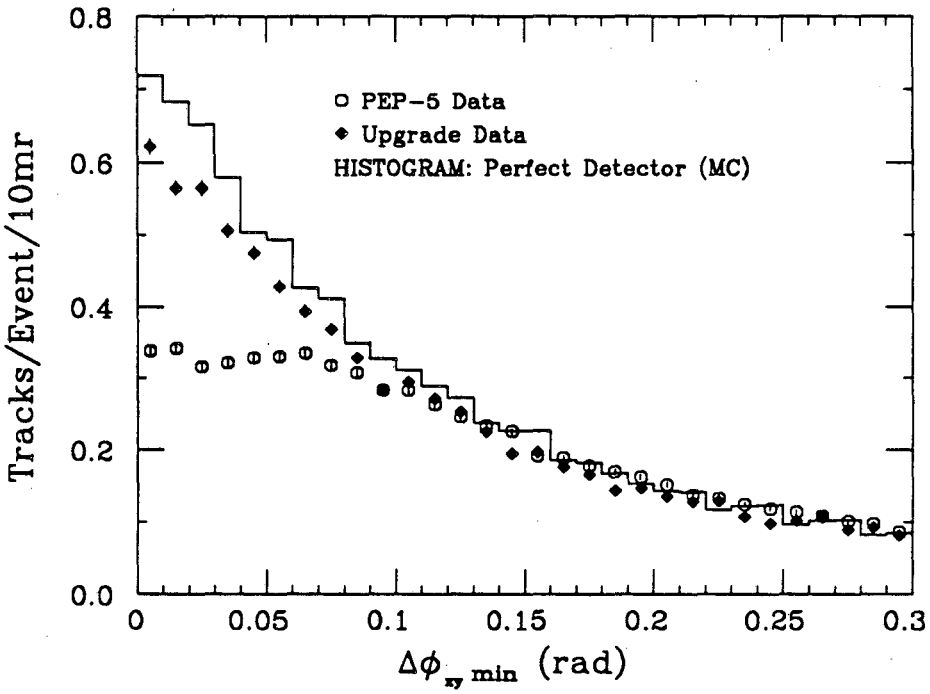

Figure A.5 Charged track angular separation distribution. *The number of tracks detected in hadronic events is plotted versus the separation in the xy projection from the nearest detected track. Data are shown for both detector configurations as well as for a Monte Carlo simulation of a fully efficient detector.*

A.2.4 Calorimetry

The location and function of the eight liquid argon (LA) calorimeter modules is described in Chapt. 3. Each module consists of 37 layers of antimony strengthened lead planes, 2 mm thick, separated by 3 mm liquid argon gaps. The layers are biased at ground or 3.5 kV in an alternating pattern. The cathode layers consist of individual strips which are instrumented for readout. The strips run in three directions: parallel to the beam (F strips), perpendicular to the beam (T strips), and at a 45° angle (U strips). F and T strips are 3.8 cm wide, while U strips are 5.4

cm wide. The total depth of a module at normal incidence is 14.5 radiation lengths, and the energy resolution is about $14\%/\sqrt{E}$ (E in GeV). The position resolution of 14.5 GeV Bhabha electrons measured to be about 7 mm.

The Upgrade end cap calorimeters (ECCs) play a relatively minor role in the present analysis; as a result of the strict $|\cos\theta|$ cuts on accepted photons, the ECCs represent only about 18% of the utilized calorimetric solid angle. Nonetheless, we discuss them in more detail because they are not described comprehensively elsewhere and because the author is especially familiar with the details of their construction, testing, and implementation.

The ECCs are constructed of 36 layers each of lead and proportional tubes. The planes of lead are each 2.8 mm thick, and the total depth is 18 radiation lengths. The annular planes of proportional tubes are have inner and outer radii of 40 cm and 146 cm, and each contains 191 tubes. The aluminum tubes are rectangular in cross section with a width of 15 mm and a depth of 9 mm. A 50 μm wire is strung through the center of each tubes and is biased at 1650 V while the tube walls are held at ground. A gas mixture of 89% argon, 10% CO_2, and 1% CH_4 ("HRS gas") is flowed constantly through the tubes.

The tube planes are oriented in 4 different directions: vertically (X), horizontally (Y), canted $+45°$ (U), and canted $-45°$ (V). The orientation of each layer is given in Table A.1. Also indicated in this table is the ganging scheme, whereby the approximately 9000 tubes in each endcap are associated into 1276 channels for read out. Tubes are ganged in depth and (in some cases) laterally as well. For example, two adjacent tubes in layer 9 will be tied to pairs of tubes in layers 13 and 17. The ganging attempts to follow a projective geometry so that all tubes in a channel approximately lie in a plane which contains the interaction point.

It is evident that the gang types in Table A.1 fall into three categories. The types in the front section ($X1, Y1, U1, V1$) are ganged by two layer in depth and are not ganged laterally. The middle section ($X2, Y2, U2, V2$) is ganged by three layers in depth and by two tubes laterally. The back section contains only two gang types

Table A.1 *Ganging pattern for the End Cap Calorimeters.*

Gang type	Layers	Transverse	Number of channels
X1	1,5	1	191
Y1	2,6	1	191
U1	3,7	1	191
V1	4,8	1	191
X2	9,13,17	2	96
Y2	10,14,18	2	96
U2	11,15,19	2	96
V2	12,16,20	2	96
X3	21,23,...,35	3	64
Y3	22,24,...,36	3	64

$(X3, Y3)$ and is ganged by eight in depth and by three laterally. The depths of the front, middle, and back sections in radiation lengths are 4, 6, and 8 respectively. A 15 GeV electron typically leaves about 30% of its energy in the front, 60% in the middle, and 10% in the back, with very little energy leaking out the back of the calorimeter.

The readout electronics of the ECCs are described thoroughly in Ref. 49. They consist of charge-sensitive preamplifiers, shaping amplifiers, sample-and-hold modules, and voltage digitizers. The system is calibrated and read out under CAMAC control.

One of the ECCs was tested in a positron beam and a pion beam before installation. The results of the positron beam test are described in Ref. 50. From that test, we show in Fig. A.6 an example of the response of the EEC to low intensity pulses of 10 GeV positrons. Clear peaks can be seen for 1-5 positrons/pulse, with an energy resolution of about $18\%/\sqrt{E}$. An extensive study of Bhabha events in the ECCs at PEP is presented in Ref. 51. An energy resolution of about $22\%/\sqrt{E}$

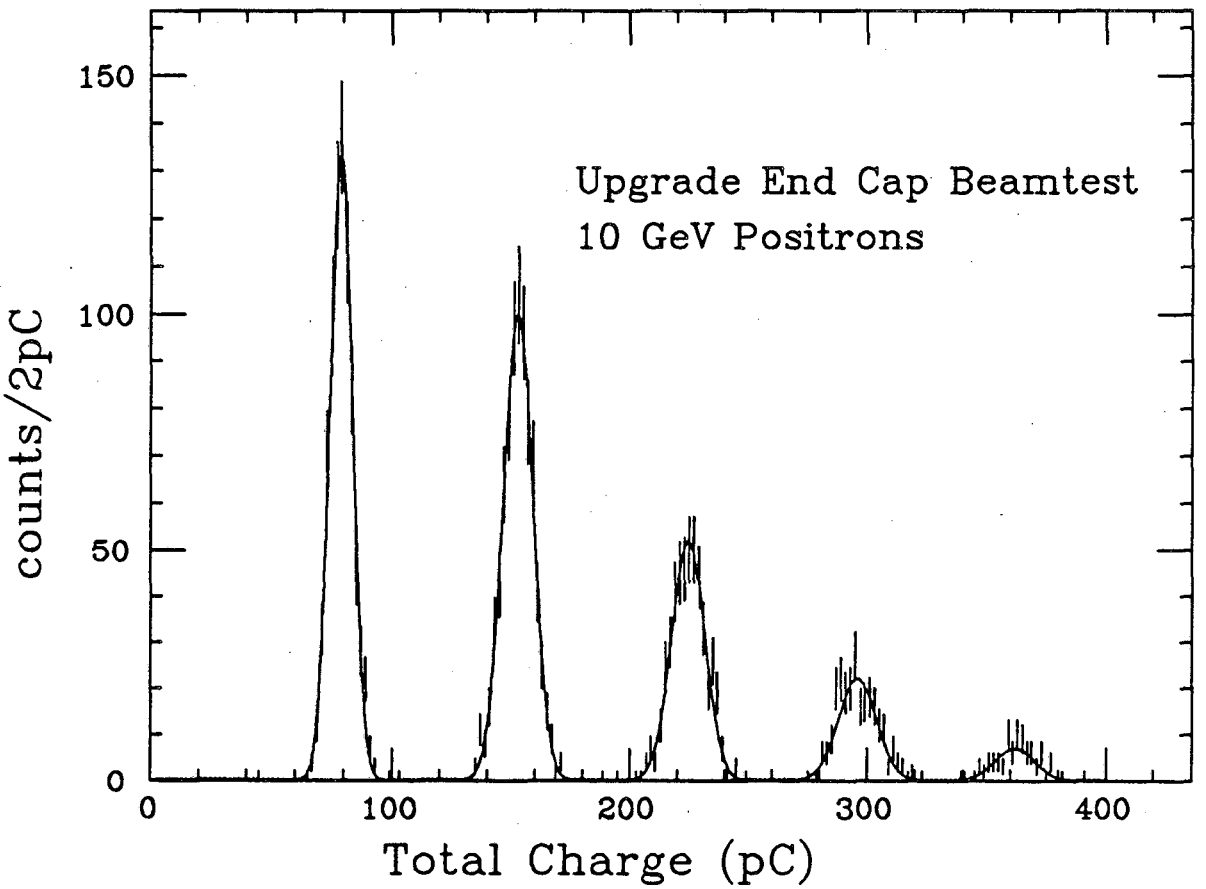

Figure A.6 Response of Upgrade End Cap Calorimeter to 10 GeV positrons. *A data sample from beam test T-356 shows a distribution of total charge collected on the calorimeter anode wires in response to pulses of small numbers (1-5) of 10 GeV positrons. This particular example used a mixture of argon and ethane and a bias potential of 1900 Volts.*

was observed.

Appendix B. Fragmentation Models

QCD gives a promising description of high-energy production of quarks and gluons. These colored partons, however, appear to be confined; we invariably observe jets of colorless hadrons rather than free quarks and gluons. The predicted increase of α_s at low Q^2 suggests a reason for this confinement, but the actual mechanism of hadronization cannot be described by perturbative QCD. For this, we must rely upon phenomenological fragmentation models.

A systematic comparison of fragmentation models is beyond the scope of this thesis; several excellent references exist on the subject.[52,37,35] Our analysis of the EEC and α_s, however, makes use of several fragmentation models, so a short discussion is included here.

B.1 General Features

A common feature of all fragmentation models is that they work in the impulse approximation. That is, hadrons are produced according to semiclassical probabilities rather than quantum mechanical amplitudes. This feature lends itself to implementation by Monte Carlo computer techniques.

In some models, a fixed order matrix element calculation is used to produce an initial configuration of quarks and gluons. The fragmentation Monte Carlo then governs the transformation of these partons into hadrons. This is true for the string and independent fragmentation models, and in each case we use the $O(\alpha_s{}^2)$ calculation of Gottschalk and Shatz[6] to generate the initial parton states. The exception to this pattern is the shower model, where the matrix element is bypassed and all secondary gluon and quark emission is handled within the Monte Carlo model.

B.2 String Fragmentation

In the string model, the QCD color field is represented as a one-dimensional

flux tube connecting the quark and antiquark. As the partons move apart, this string is stretched and it breaks by creating $q\bar{q}$ pairs through a tunneling process. The longitudinal momenta of hadrons (along the string direction) is distributed according to a fragmentation function $f(z)$, where z is the fraction of $(E+p_{||})$ carried by the hadron. Hadrons obtain transverse momentum according to a Gaussian distribution of width σ_q. Additional parameters control the relative abundance of strange particles, baryons, and vector mesons. Momentum, energy, and all internal quantum numbers are conserved at each breaking of the string.

We use the Lund String Model of Andersson *et al.*,[40] with the Symmetric Lund fragmentation function

$$f(z) = \frac{1}{z}(1-z)^A \exp -(Bm_\perp^2/z). \qquad (B.1)$$

The model is tuned to fit the data by a detailed comparison of its predictions with a variety of observed distributions, including sphericity, thrust, aplanarity, $p_\perp$, $p_\perp^{in}$, $p_\perp^{out}$, and rapidity.[35] Neither the EEC nor the EECA is considered in the selection of any parameters except Λ, which is determined from α_s as described in Chapt. 6. The parameter values used are summarized in Table B.1.

Table B.1 Parameters for fragmentation models.

	Lund String	IF (Ali)	IF(Hoyer)	Lund Shower
y_{min}	0.015	0.015	0.015	—
Q_0	—	—	—	1.0 GeV
σ_q	265 MeV	285 MeV	295 MeV	230 MeV
A	0.90	0.75	1.10	0.45
B	0.7 GeV^{-2}	0.7 GeV^{-2}	0.7 GeV^{-2}	0.9 GeV^{-2}
$\Lambda_{\overline{MS}}$	330 MeV	150 MeV	23 MeV	—
Λ_{LLA}	—	—	—	390 MeV

In the string model, a gluon is represented as a transverse excitation or kink in the color string connecting the quark and antiquark. This scheme accommodates arbitrarily soft gluons smoothly into fragmentation process; there is no abrupt discontinuity between soft gluon emission and no gluon emission.

An additional consequence of this treatment of gluons is the "string effect", where the density of particles is depleted between the quark and antiquark jets in three-jet events, as shown in Fig. B.1. The observation of this phenomenon in e^+e^- data[37,38] was a triumph for the string model, and it was shown subsequently that the same effect can be obtained in QCD by considering the destructive interference among the color fields of the quark, antiquark and gluon.[53] For our purposes, it is important to note that since the string effect makes three-jet events appear more like two-jet events, a higher value of α_s is required for models which include this feature.[17]

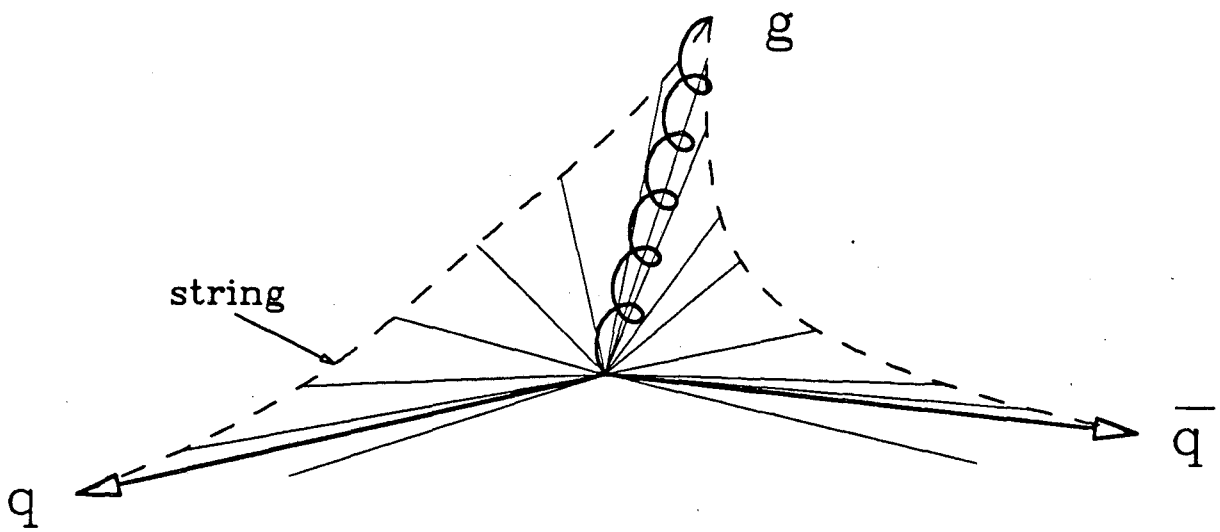

Figure B.1 A schematic illustration of string fragmentation. *The configuration of partons (heavy lines), string (dashed line), and final state particles (thin lines) in a three-jet event are sketched in momentum space.*

B.3 Independent Fragmentation Models

In independent fragmentation (IF) models, each parton fragments individually according to the general method of Feynman and Field.[54] This process is illustrated

in Fig. B.2. The initial quark q_0 pulls a pair $\bar{q}_1 q_1$ from the vacuum and forms a meson with $\bar{q}_1$. The remaining quark q_1 hadronizes in the same way, and the fragmentation proceeds recursively until the remaining quark has very low energy. As in the string model, the longitudinal momenta are obtained from a fragmentation function, and the transverse momenta have a Gaussian distribution.

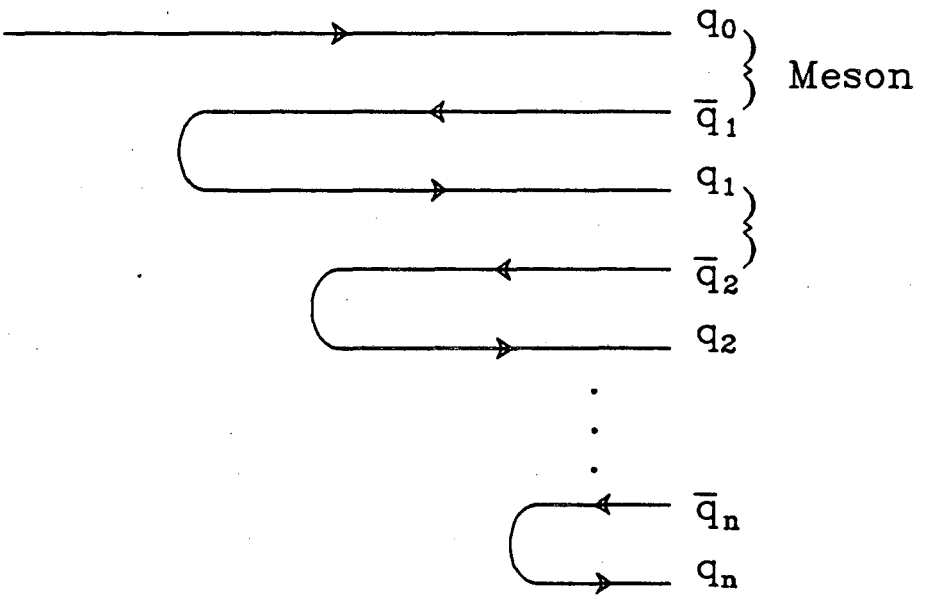

Figure B.2 *A schematic illustration of independent fragmentation.*

Energy and momentum are not conserved in the intermediate steps of the IF process. The momenta of the final state particles must be adjusted somehow at the end to coincide with the energy of the original parton system. There are several schemes for accomplishing this and we examine the two most common, those of Ali and Hoyer. The method chosen makes little difference in two-jet events, but in three-jet events it can have significant effects.

The Hoyer method is designed to preserve the directions of the parton jets. After fragmentation, the particle momenta are rescaled in each jet to conserve transverse momentum locally. Then the longitudinal momentum of each jet is rescaled to reflect the momentum ratios of the original partons. Finally, the entire event energy is scaled to the original center-of-mass energy. Thus in three-jet events, the lowest energy jet (usually the gluon) tends to have its energy increased, so the

events appear even more three-jet like.

In the Ali scheme, the momentum is balanced by boosting the event to its new rest frame. All of the particle energies are then rescaled to get the correct center-of-mass energy. The purpose here is to preserve the relative energy of the jets.

We implement the IF models within the Lund Monte Carlo package, and we use the same form of the fragmentation function (Symmetric Lund). The parameter B is fixed at 0.7 GeV^{-2}, and the parameters A, σ_q and $\Lambda_{\overline{MS}}$ are chosen to fit the average charged multiplicity, the $p_\perp^{out}$ spectrum, and the EECA (for $\chi > 28.8°$). The parameter values used are shown in Table B.1.

It should be emphasized that the IF models have serious faults. They lack Lorentz covariance, they do not easily accommodate soft partons, and they are strongly disfavored by the data in certain regions.[52] Indeed, they fail to describe the EEC. Consequently, results from IF models are presented only for comparison, and they should not be assigned the same weight as the other results.

B.4 Shower Models

The most recent and potentially most successful models of hadronization employ the leading log approximation (LLA) to generate a shower of quarks and gluons. Each event begins with the highly excited $q\bar{q}$ pair, and a shower is generated by successive use of the basic $q \to qg$, $g \to gg$ and $g \to q\bar{q}$ splittings. This process is shown schematically in Fig. B.3. The LLA sums all orders of α_s but retains only the most singular piece. This allows an arbitrary number of splittings to occur. The shower continues until the mass of each parton drops below some cutoff Q_0. At this point the various models diverge; some split all of the remaining gluons into $q\bar{q}$ pairs, form low-mass colorless clusters, and let them decay into hadrons via phase space (*e.g.* Webber[55]) or via a parameterization of low energy data (Gottschalk[56]). In the Lund shower model,[31] the each colorless system of quarks and gluons is replaced by a string, and fragmentation proceeds in the usual manner.

In a parton shower, the probability that a branching $a \to bc$ will take place in

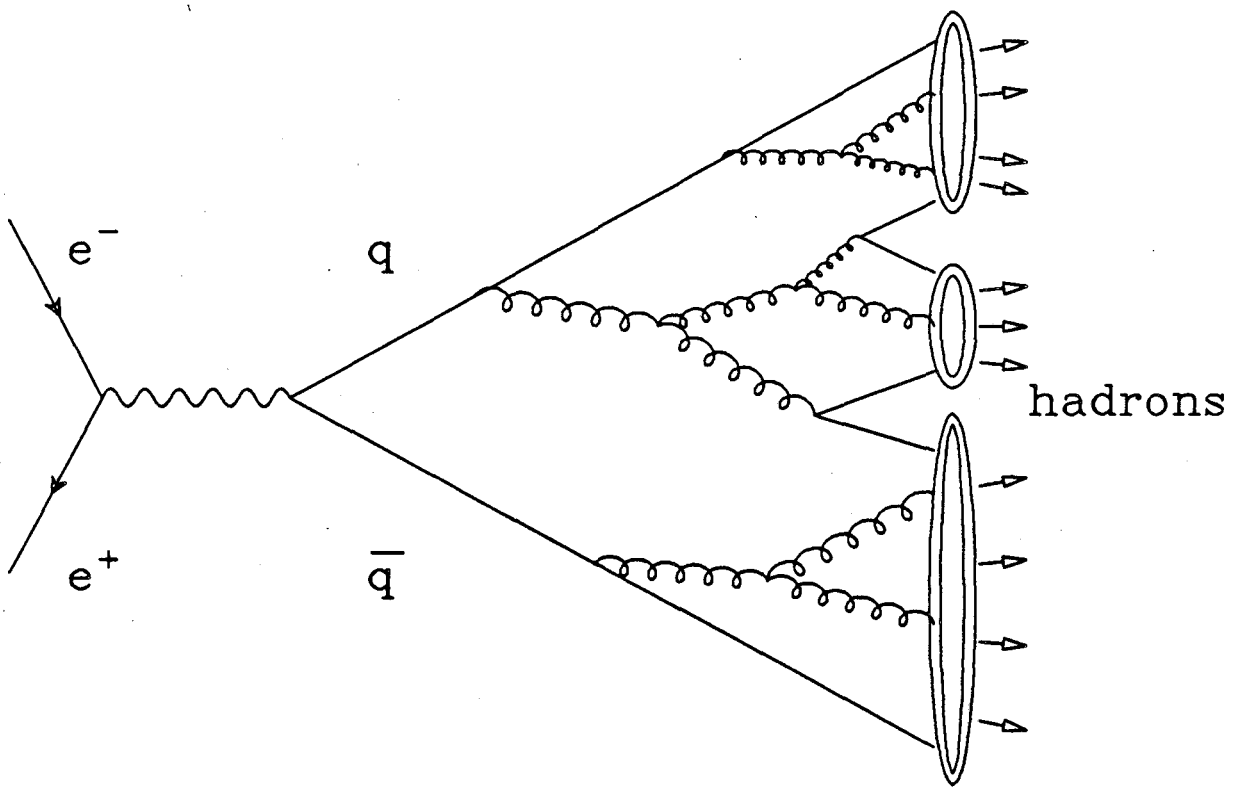

Figure B.3 A schematic illustration of shower fragmentation. *The diagram depicts the evolution of a $q\bar{q}$ pair into hadrons in a leading-log shower model. The ellipses represent string fragmentation or some clustering and decay scheme, depending on the specific model.*

an interval dt, where $t = \ln(m_a^2/\Lambda^2)$, is given by the Altarelli-Parisi equations

$$\frac{dP_{a\to bc}}{dt} = \int dz \frac{\alpha_s(Q^2)}{2\pi} P_{a\to bc}(z). \qquad (B.2)$$

Note that $\alpha_s(Q^2)$ is determined individually at each branching by $\alpha_s(Q^2) = 12\pi/((33 - 2N_f)\ln(Q^2/\Lambda_{LLA}))$ where $Q^2 = z(1-z)m_a^2$. Consequently, the coupling strength in shower models is not governed by a fixed $\alpha_s(E_{cm}^2)$ as in matrix element calculations, but rather by Λ_{LLA} which characterizes a running α_s. Thus, the concept of a running coupling constant is inherent in the shower model. The authors of the Lund Shower Model warn against direct comparison of Λ_{LLA} and $\Lambda_{\overline{MS}}$ as too naïve,[57] however.

We use the shower model of the Lund group.[31] It is tuned to fit our data in the same manner as the Lund (matrix element) String model. The parameter values used are shown in Table B.1, and they produce very good agreement with the data.[35] This particular version of the Lund shower model includes coherence effects via angular ordering[55] and first order matrix element weighting of the first branching.

Appendix C. Details of Data Correction

In chapter 5, we describe the correction procedure which we apply to our EEC and EECA distributions. This two-step procedure gives us partially corrected data ($C_1 \cdot \mathrm{EECA}_{data}(\chi)$) from which we determine α_s, and fully corrected data (*e.g.* $C_1 \cdot C_2 \cdot \mathrm{EECA}_{data}(\chi)$) which we compare directly to the data from other experiments. In this appendix, we give additional details of the method and some further motivation for carrying out the corrections in this way.

C.1 General Method

CELLO,[11] JADE,[12] TASSO,[13] MAC[14] and PLUTO[16] have used fully corrected EECA distributions to measure α_s. These groups remove the detector dependence from their data with factors determined from a Monte Carlo, then compare the corrected data with additional Monte Carlo at the four-vector level. This has the great advantage that the Monte Carlo used in the second step does not need to include the detector simulation and therefore requires relatively little computer time.*

This method has come under criticism from Min Chen of the Mark-J collaboration.[28] The approach used by Mark-J[15] is to correct the theory for experimental effects (via a Monte Carlo simulation), then compare it to the uncorrected data. This latter method is in principle more rigorous. For example, in a measurement of α_s, the detector effects are recalculated for each test value of α_s. In the first method, the Monte Carlo from which the corrections are determined contains some initial guess for the value of α_s, and this introduces an potential source of bias in the measurement. This problem is discussed in detail in Ref. 28.

We adopt an intermediate approach through the use of partial corrections. In the α_s measurement, we compare the partially corrected data to acceptance cor-

* For example, the full Mark II detector simulation and event reconstruction is approximately 70 times slower than the hadronic event generation alone.

rected (AC) Monte Carlo which includes, on an event-by-event, particle-by-particle basis, the gross corrections for detector effects and initial state radiation. (The three modes of the Monte Carlo simulation are described in Table C.1.) The partial corrections we apply to the data (C_1) are relatively insensitive to the model assumptions, so much of the rigor of the Mark-J method is retained.

Table C.1 Properties of the Monte Carlo. *The table indicates which features are included in the three levels of the Monte Carlo simulation.*

	QCD and Fragmentation	Initial State Radiation	Solid Angle Cuts	Lost Particles (n's, ν's...)	Track and Event Cuts	Efficiency and Resolution
GEN	yes	no	no	no	no	no
AC	yes	yes	yes	yes	yes	no
FS	yes	yes	yes	yes	yes	yes

In addition, we calculate the large correction factors C_2 and apply them to the data to form fully corrected distributions. This step is entirely divorced from the α_s determination, but we carry it out because the resulting distributions are interesting in their own right. This allows us to make meaningful comparisons of our EEC and EECA with other experiments. Also, the fully corrected data can be compared directly with theoretical predictions, which is especially useful in QCD because the calculations and fragmentation models are undergoing constant improvement.

C.2 Errors on C_1 and C_2

The Monte Carlo samples from which C_1 is determined are listed in Table C.2. All of these samples give reasonable agreement with the observed EEC and EECA, and there are no significant differences in the correction factors determined from each model separately.

We estimate the systematic errors on C_1 by comparing two subsamples of these FS Monte Carlo sets: low multiplicity ($N_{ch} \leq 10$) and high multiplicity ($N_{ch} \geq$

Table C.2 Monte Carlo samples for C_1 calculations.

Detector	M.C. Model	Matrix Elem.	Events	α_s	Λ_{LLA}
PEP-5	Lund String	GKS	100,000	0.173	—
Upgrade	Lund String	GKS	10,000	0.173	—
	Lund String	GS	20,000	0.150	—
	Webber Shower	—	10,000	—	—
	Lund Shower	—	10,000	—	500 MeV
	Lund Shower	—	10,000	—	400 MeV

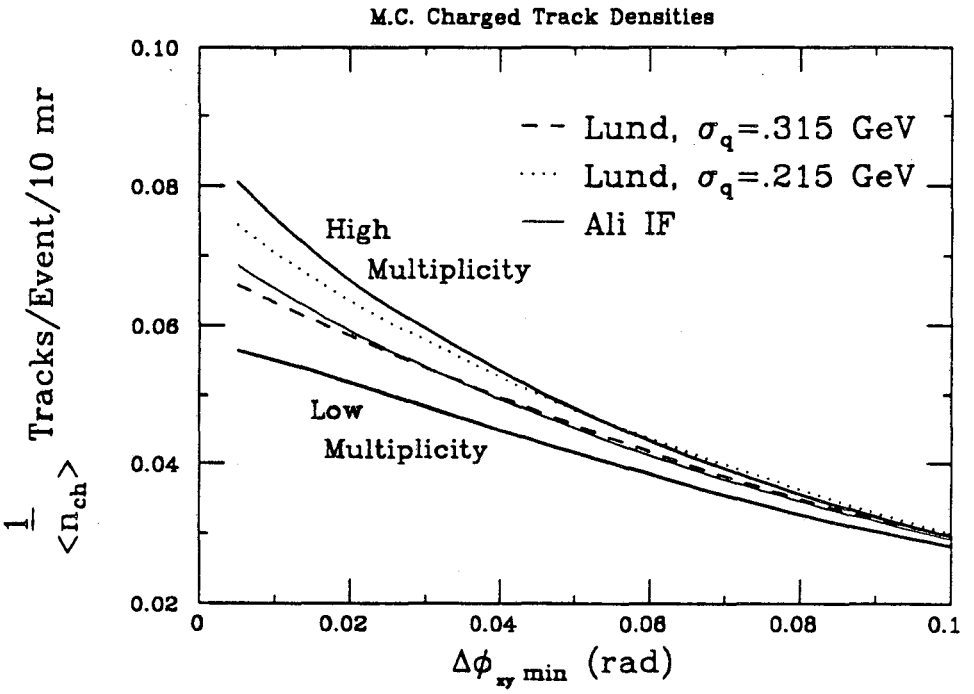

Figure C.1 Azimuthal charged track densities for various Monte Carlo samples. *The closest track distribution (see Fig. A.5) is shown for five different Monte Carlo samples. For each sample, the curves have been normalized to the average event multiplicity.*

16). The purpose of this decomposition is to compare the detector corrections for different track densities. Figure C.1 shows that these samples give conservative extremes for the possible track densities that actually occur in hadronic events. The

C_1 factors are calculated separately with the high and low multiplicity subsamples. In Fig. C.2 we show the standard deviation between the two calculations for each bin in χ. For the EECA, we use as our estimate of the errors on C_1 the sum in quadrature of these deviations and the statistical errors from the Monte Carlo. For the EEC correction factors, the error from Monte Carlo statistics is negligible.

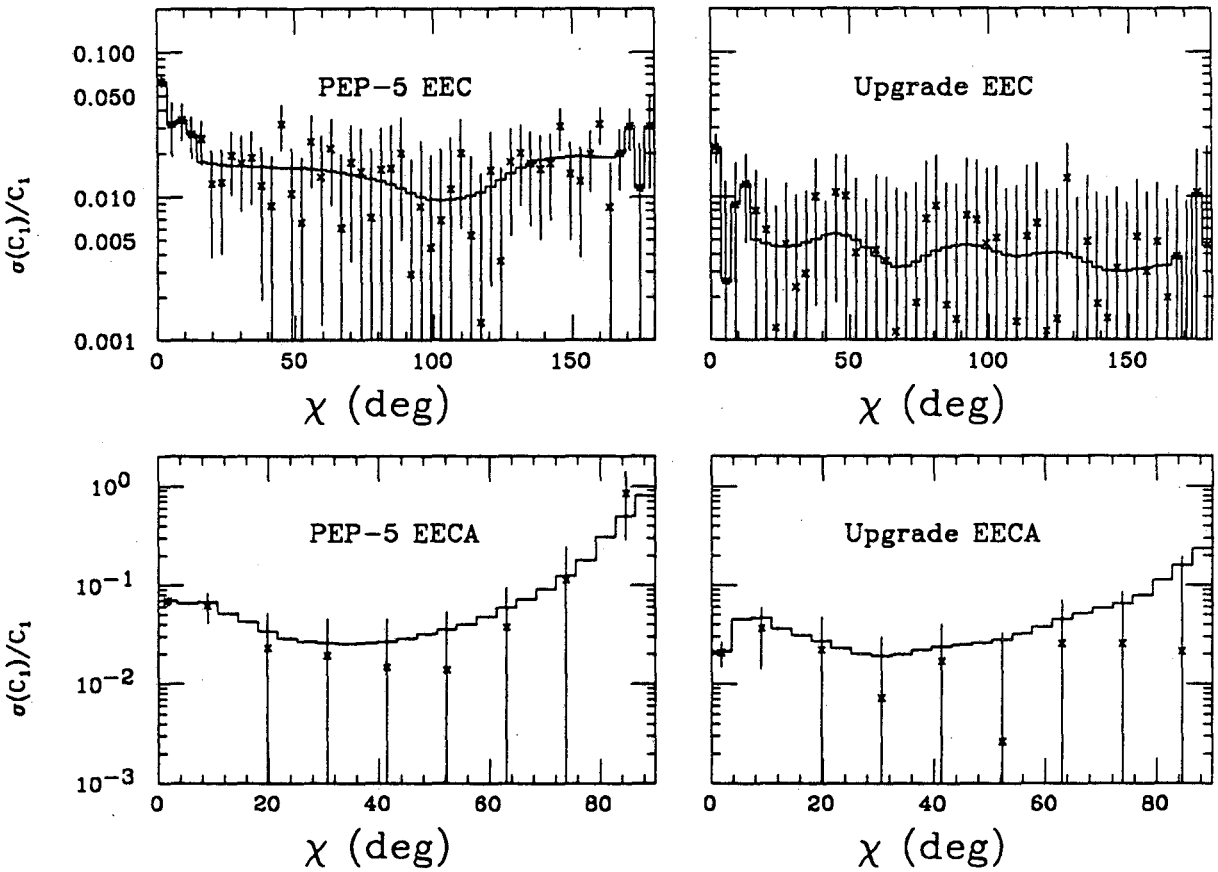

Figure C.2 **Estimated errors on C_1.** *The points show the standard deviation in C_1 from a comparison of the high and low multiplicity Monte Carlo samples. The error bars represent the statistical uncertainties on the deviations. For the EECA, the data are rebinned into larger intervals (10.8°) before comparison. The histograms show the level of systematic error that we assign to C_1.*

The uncertainties in C_2 arise from sensitivity to the fragmentation models and QCD parameters, so the errors on C_2 are estimated from comparisons with

two alternative models (Hoyer IF and Lund Shower) and the two-sigma upper and lower limits of α_s in the Lund String model. The standard deviation on the C_2 factors computed from these four samples is shown in Fig. C.3. The contributions from Monte Carlo statistics to the final systematic errors on C_2 are negligible.

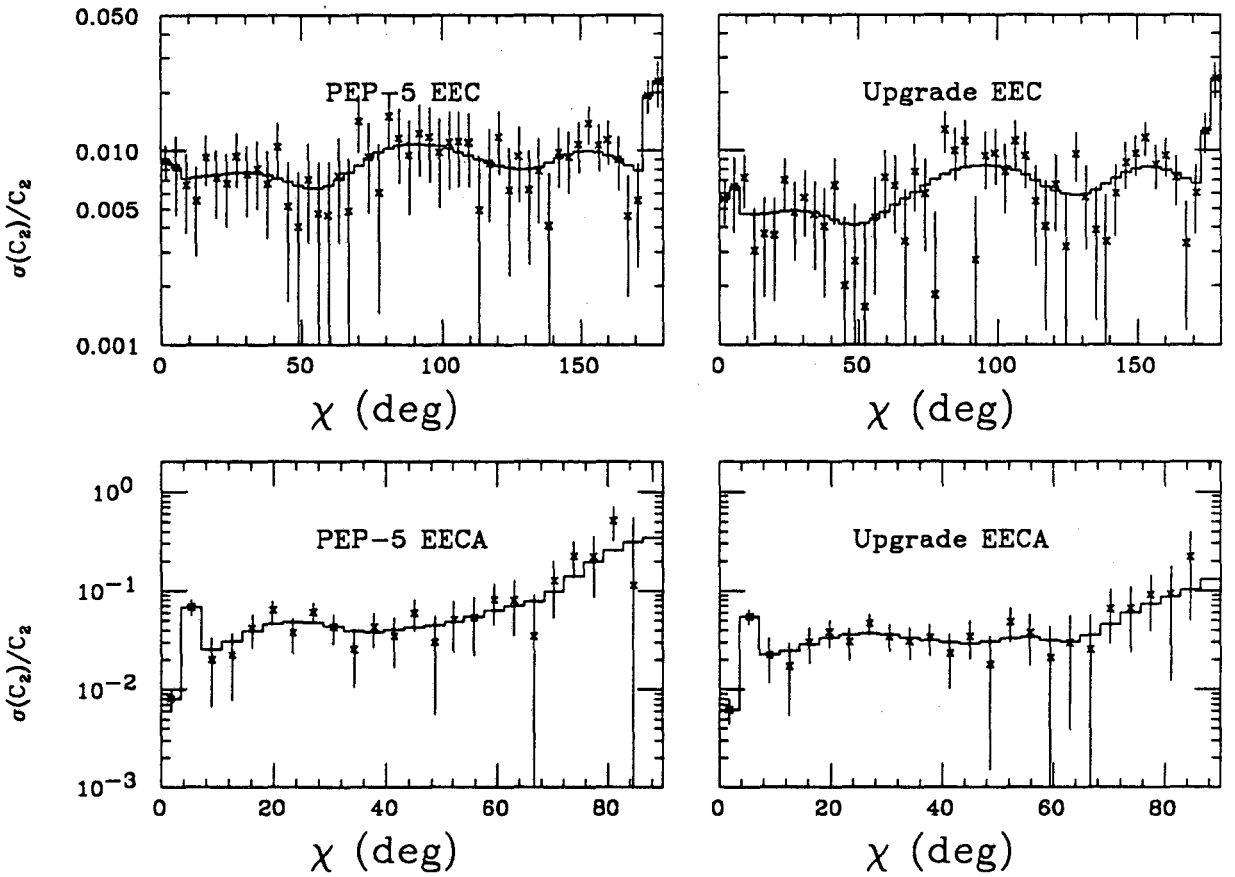

Figure C.3 Estimated errors on C_2. *The points show the standard deviation in C_2 from a comparison of four different Monte Carlo samples (described in the text). The error bars represent the statistical uncertainties on the deviations. The histograms show the level of systematic error that we assign to C_2.*

Finally, recall that the EEC and EECA are corrected separately. A corrected EECA may also be obtained from the asymmetry of the corrected EEC. The systematic errors in the EECA obtained in this way are larger, but the two methods agree well, as shown in Fig. C.4.

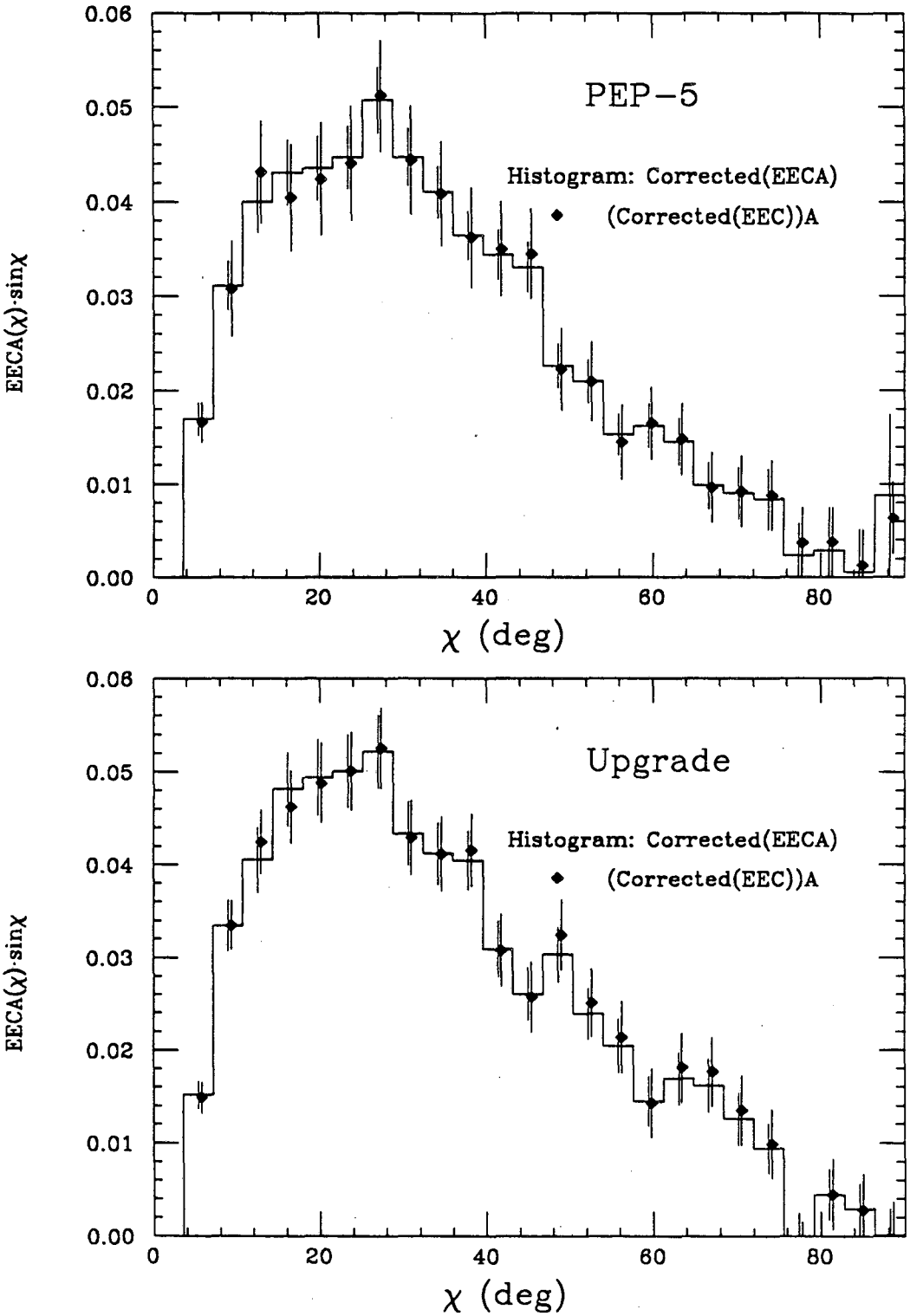

Figure C.4 Comparison of different methods for correcting the EECA. *The EECA obtained from direct corrections is shown in the histograms. The points show the asymmetries of the corrected EEC distributions.*

C.3 α_s DEPENDENCE

We return to the question of the influence on the α_s measurement of the α_s value used in the correction Monte Carlo. We make an explicit check for this bias by examining the correction factors for the EECA integrated over the entire range of χ used in the α_s measurement, in the same manner as Ref. 28:

$$C_1 = \frac{\int_{28.8^\circ}^{90^\circ} \mathrm{EECA}_{AC}(\chi)d\chi}{\int_{28.8^\circ}^{90^\circ} \mathrm{EECA}_{FS}(\chi)d\chi},$$

$$C_2 = \frac{\int_{28.8^\circ}^{90^\circ} \mathrm{EECA}_{GEN}(\chi)d\chi}{\int_{28.8^\circ}^{90^\circ} \mathrm{EECA}_{AC}(\chi)d\chi},$$

$$C_{tot} = C_1 C_2.$$

We perform a straight-forward computation of C_2 from Monte Carlo samples generated with several different values of α_s from 0.11 to 0.20. This direct approach is not suitable for C_1 because too much computer time is required to carry out complete detector simulations for each sample which goes into the C_1 calculation. Consequently, we construct samples which mock these α_s values by re-weighting the two-, three-, and four-jet components of the large FS Monte Carlo sets. The criterion for assigning jet number is based on a y_{min} cut of 0.004 applied to the underlying parton four-vectors. The appropriate weights of the *n-jet* components are determined from the GS matrix element and are shown in Table C.3. below.

Table C.3 Monte Carlo multi-jet fractions.

α_s	2-jet fraction	3-jet fraction	$\geq$4-jet fraction
0.114	0.618	0.371	0.011
0.140	0.509	0.474	0.017
0.173	0.374	0.603	0.023
0.199	0.272	0.695	0.033

The results of this study are shown in Fig. C.5. C_1 changes by less than 1% over this entire range of α_s. There is an appreciable change in C_{tot} and it follows the same trend as the solid curve from Ref. 28, although the sensitivity is considerably smaller.† We emphasize that our measurement of α_s is made by comparing theory and data at the AC level, so this latter change does not affect the α_s value obtained and no bias is introduced other than the tiny effect on C_1.

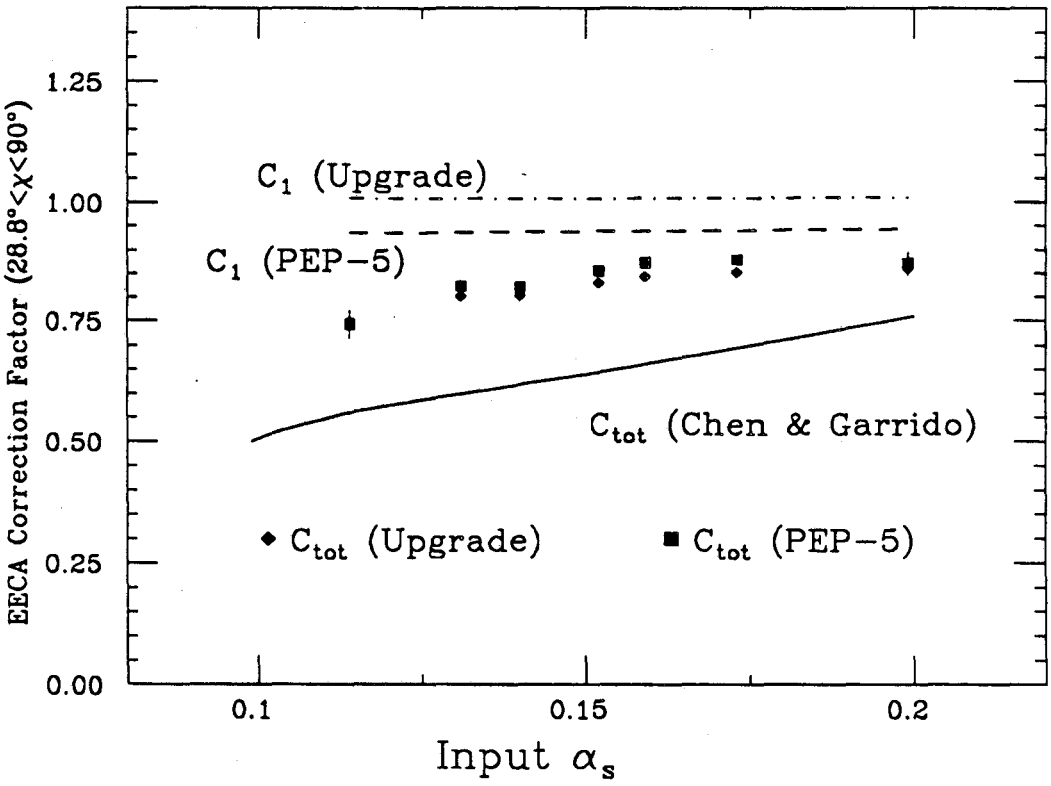

Figure C.5 Correction Factors vs. α_s. *The correction factors for the EECA integrated from 28.8° to 90° are shown as a function of α_s. The errors on C_{tot} are from Monte Carlo statistics. The solid curve is reproduced from Ref. 28, and represents different detector properties and event selection cuts.*

† The Chen and Garrido curve is based upon a different set of detector parameters and cuts, presumably those of Mark-J.

Appendix D. Survey of Recent α_s Measurements

As we discuss in the preface, the measurement of α_s presents serious theoretical and experimental difficulties. This is evident in Fig. D.1, which shows the widely varying values of α_s presented in 1983.[58] Since that time, there has been considerable effort in both experiment and theory, and a more consistent picture has emerged.

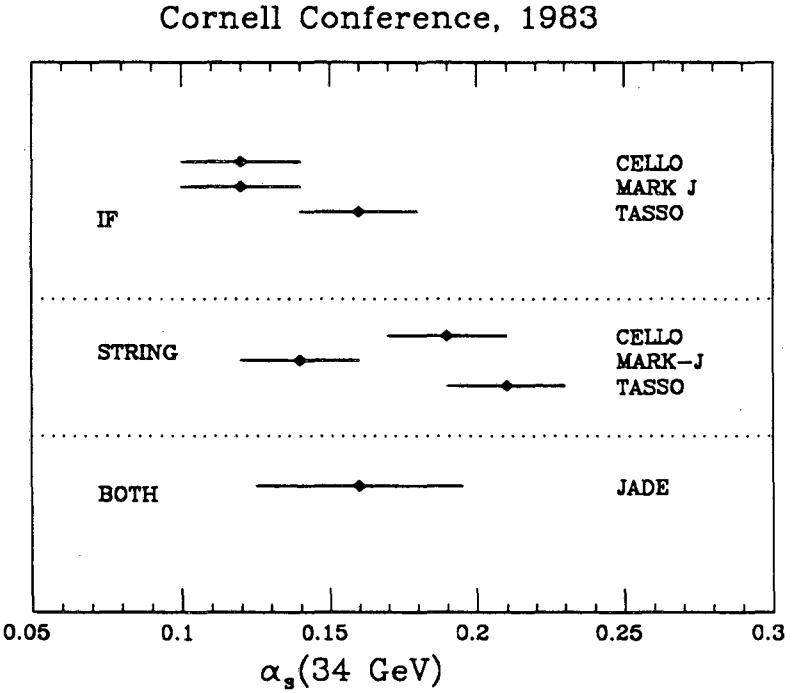

Figure D.1 α_s **measurements in 1983.** *We show the* α_s *measurement from PETRA presented in the Lepton Photon Conference at Cornell.*

D.1 α_s MEASUREMENTS FROM THE EECA

Some recent EECA determinations of α_s were discussed in chapter 6. A broader sampling of these results is shown in Fig. D.2, where they are grouped according to matrix element calculation and fragmentation model assumed in the analyses.

Systematic differences are quite evident. The string models give higher values (~20%) than the IF, and FKSS/GKS gives higher results (~15%) than ERT. The

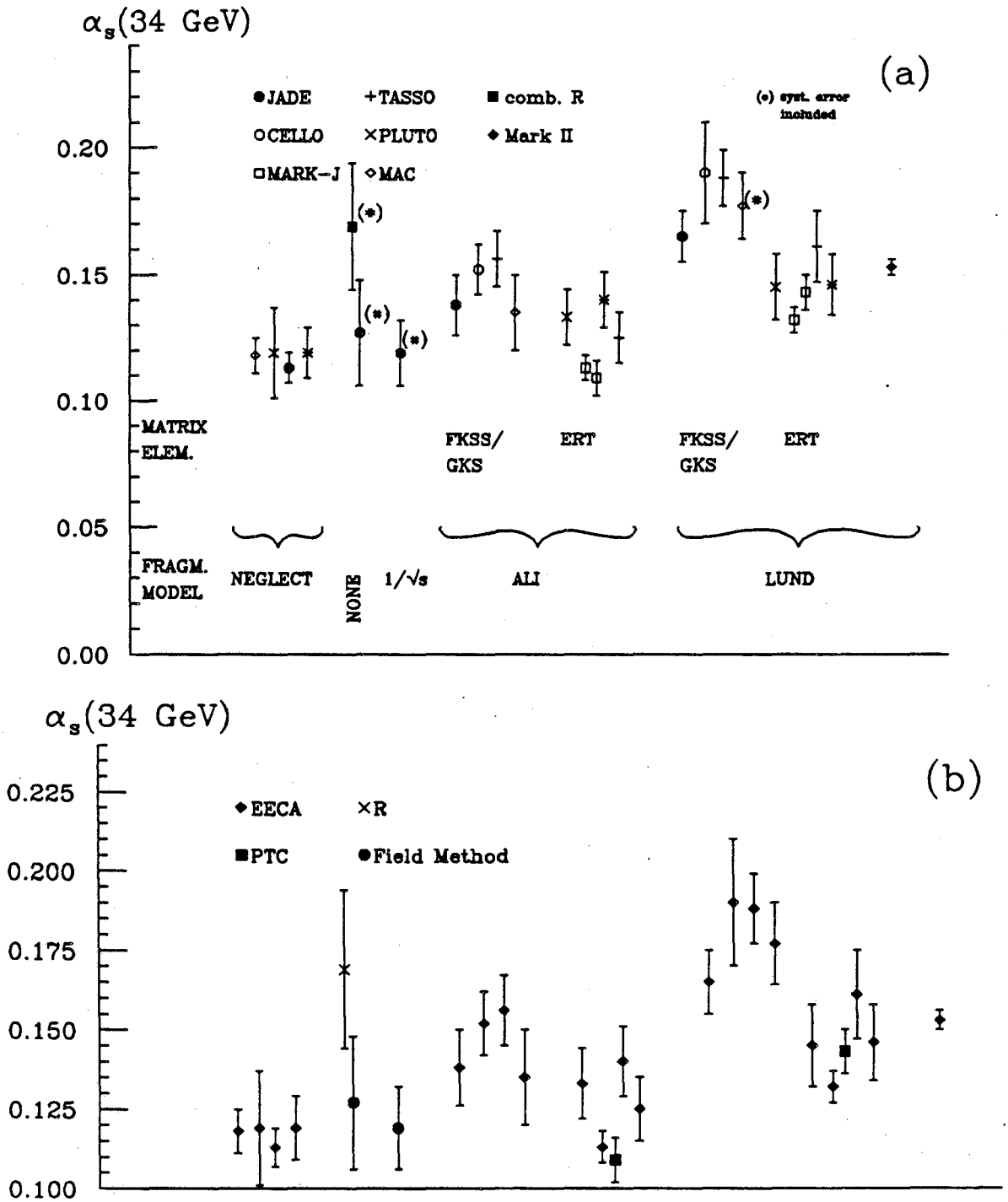

Figure D.2 α_s **measurements from PEP and PETRA.** *This summary of* α_s *results was presented at the 1986 ICHEP in Berkeley,*[59] *except for the new result on the right. In (a), the plot symbols indicate the experimental groups who report these values. Each measurement appears at same abscissa in (b), but here the plot symbols correspond to the method used for determining* α_s*. The Planar Triple Correlation (PTC) and Field Method are described in Ref. 59. Errors are statistical only unless noted otherwise.*

matrix element sensitivity has been explained the different methods employed for jet dressing. As $y_{min} \to 0$, these differences vanish, but even at $y_{min} = 0.01 - 0.04$ they change the three-jet rate by 10%-15%.[6] The Gottschalk and Shatz (GS) have recalculated the dressed matrix element and have included subleading corrections that were neglected in previous calculations. The present result, the only measurement which employs GS matrix element, gives better agreement with the ERT values than with the GKS. In addition, there appears to be a systematic trend associated with the choice of fragmentation model; string models generally give higher values of α_s than IF models. This fragmentation dependence is understood, as least qualitatively, in terms of the way energy-momentum conservation is handled in the various schemes (see App. B).

If these differences are allowed for, the agreement between the various experiments is quite good, as is expected from the good agreement among the corrected EECAs (see Fig. 5.5). This tends to indicate that the remaining ambiguities in the measurement are not due to experimental problems, but rather to theoretical subtleties.

D.2 OTHER α_s MEASUREMENTS IN e^+e^- EXPERIMENTS.

D.2.1 R Measurement

Away from resonances, α_s may be determined from the relative rate of hadronic events, $R = \frac{\sigma(e^+e^- \to hadrons)}{\sigma(e^+e^- \to \mu^+\mu^-)}$. Above $b\bar{b}$ threshold, the Quark Parton Model (QPM) predicts R=11/3, and $O({\alpha_s}^2)$ QCD corrections give

$$R = \frac{11}{3}\left(1 + \frac{\alpha_s}{\pi} + 1.4\left(\frac{\alpha_s}{\pi}\right)^2\right),$$

so a precise measurement of R determines α_s. Such determinations have been made by CELLO,HRS, JADE, MAC, MARK-J, PLUTO, and TASSO. A combined fit[60] to all of the R values yields α_s(34 GeV)=0.169 $\pm$ 0.025, and this result is included in Fig. D.2.

An R measurement is an attractive way to determine α_s because the QCD prediction does not depend on jet dressing schemes or fragmentation effects. Un-

fortunately, R depends rather weakly on α_s, so even small errors on R lead to large uncertainties in α_s.

D.2.2 Quarkonium Decays

At lower energies, measurements of α_s are obtained from studies of the decays of heavy quarkonium states such as the Υ. The most common decay mode of $\Upsilon \rightarrow$ *hadrons* is via three gluons, as shown in Fig. D.3(a). Thus, $\Gamma(\Upsilon \rightarrow ggg)/\Gamma(\Upsilon \rightarrow \mu^+\mu^-) \propto {\alpha_s}^3$ at lowest order so α_s may be measured from the hadronic width of the Υ. In addition, the Υ can decay via a photon and two gluons, as shown in Fig. D.3(b), so

$$\frac{\Gamma(\Upsilon \rightarrow ggg)}{\Gamma(\Upsilon \rightarrow \gamma gg)} \approx \frac{5}{4}\frac{\alpha_s}{\alpha}.$$

The same statement hold for the charmonium states, and we summarize the status of these measurements in Table D.1. The precision of these α_s values is now quite good, but the renormalization scheme and the definition of Q^2 in these decays are different than in e^+e^- annihilation in the continuum, so direct comparison with the values from PEP and PETRA should be viewed with caution.

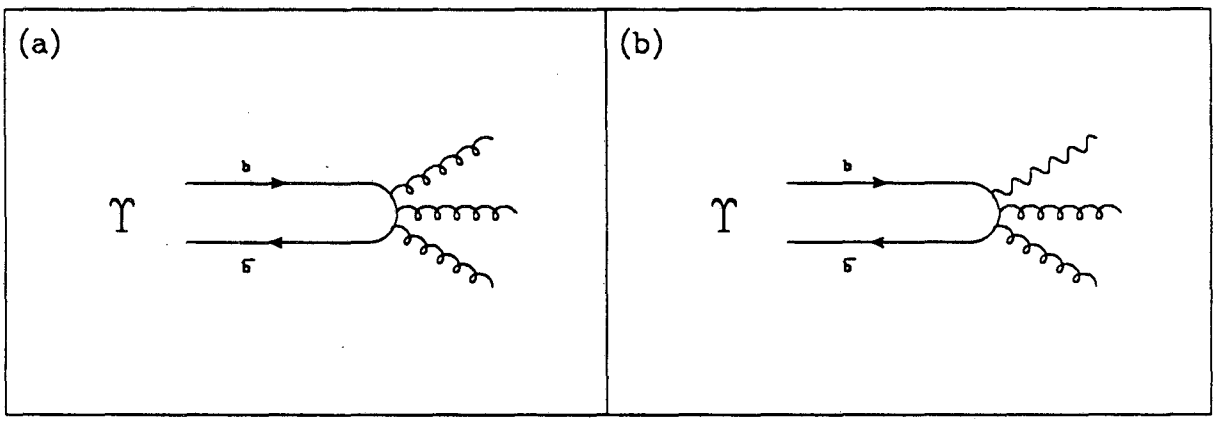

Figure D.3 Diagrams for Upsilon decay. *(a)* $\Upsilon \rightarrow$ *3 gluons, (b)* $\Upsilon \rightarrow \gamma gg$.

D.3 $\Lambda_{\overline{MS}}$ MEASUREMENTS IN OTHER TYPES OF EXPERIMENTS

D.3.1 Deep Inelastic Scattering

Another type of experiment which commonly yields measurements of $\Lambda_{\overline{MS}}$ (or of α_s at fixed Q^2) is deep inelastic scattering (DIS). Here, a virtual photon (or

Table D.1 α_s**values from quarkonium decays.**

Mode	Q^2	α_s
$\frac{\Gamma(\eta_c \to gg)}{\Gamma(\eta_c \to \gamma\gamma)}$	m_c^2	$0.20^{+0.05}_{-0.06}$
$\frac{\Gamma(J/\Psi \to ggg)}{\Gamma(J/\Psi \to \mu\mu)}$	m_c^2	$0.179^{+0.007}_{-0.009}$
$\frac{\Gamma(J/\Psi \to \gamma gg)}{\Gamma(J/\Psi \to ggg)}$	m_c^2	$0.20^{+0.10}_{-0.05}$
$\frac{\Gamma(\chi_{c2} \to gg)}{\Gamma(\chi_{c2} \to \gamma\gamma)}$	m_c^2	$0.20^{+0.10}_{-0.05}$
Average	m_c^2	0.180 ± 0.008
$\frac{\Gamma(\Upsilon \to ggg)}{\Gamma(\Upsilon \to \mu\mu)}$	m_b^2	$0.171^{+0.004}_{-0.005}$
$\frac{\Gamma(\Upsilon \to \gamma gg)}{\Gamma(\Upsilon \to ggg)}$	m_b^2	$0.178^{+0.009}_{-0.008}$
Average	m_b^2	0.173 ± 0.004

$W^{\pm}$ or Z^0) with four-momentum q ($Q^2 = -q^2$), is produced by a scattered lepton and probes a target (usually a nucleon). The experiments measure the structure functions $F(x, Q^2)$, which are related to the momentum distribution of the quarks within the target. At high Q^2, the emission of virtual gluons will soften the quark momenta and thus alter the structure functions. More precisely, QCD predicts that for fixed x, $dF/d\ln Q^2 \propto \alpha_s$. As an example, the BCDMS collaboration[61] has studied muon-carbon scattering in the range 50 GeV^2 $\leq Q^2 \leq$150 GeV^2, and reports α_s(Q=10 GeV)=$0.160 \pm 0.003 \pm 0.010$.

D.3.2 Two-photon Scattering

The structure function F_2^{γ} of the photon is also sensitive to α_s. The pointlike contribution to F_2^{γ} is, in fact, absolutely calculable in perturbative QCD so the absolute magnitude of the structure function (not just its Q^2 dependence) may be used to determine α_s. Recent $\Lambda_{\overline{MS}}$ measurements[62] from F_2^{γ} are summarized in Table D.2. An average value[62] of $\Lambda_{\overline{MS}}=195^{+60}_{-40}$ (systematics included) corresponds to $\alpha_s(34\ \text{GeV})=0.138^{+.007}_{-.005}$, which is reasonably close to the recent e^+e^- values. It should be noted that some theoretical uncertainty exists in separating the pointlike

and hadronic components of F_2^γ, so the precision of these measurements may be overly optimistic.[63]

Table D.2 $\Lambda_{\overline{MS}}$ **values from two-gamma scattering.** *The multiple values reported by some experiments reflect different model assumptions.*

Experiment	$Q^2(\mathrm{GeV}^2)$	$\Lambda_{\overline{MS}}$ (MeV)
PLUTO	3-100	183^{+80}_{-54}
JADE	10-220	250 ± 90
TASSO	7-70	140^{+190}_{-60}
PLUTO	3-100	240 ± 90
PLUTO	3-100	160 ± 60
TPC/2γ	4-7	257 ± 92
TPC/2γ	4-7	133 ± 50

D.3.3 Hadron Collisions

Quite recently, groups from hadron colliders have reported values of α_s from the ratio of 3-jet to 2-jet production observed in their detectors. At present, there are large theoretical uncertainties in these determinations, and they have been absorbed into the factors K_3 and K_2. These factors are calculable in principle, but have not been calculated. The ratio K_3/K_2 is expected to be near unity, however. The UA2 collaboration reports[64] $(K_3/K_2)\alpha_s = 0.23 \pm 0.01 \pm 0.04$ for $\langle Q^2 \rangle \sim 1700$ GeV^2. The same value, $(K_3/K_2)\alpha_s = 0.23 \pm 0.01 \pm 0.04$, is reported by the UA1 group[65] for $\langle Q^2 \rangle \sim 4000$ GeV^2. These results are difficult to interpret quantitatively because of the unknown K-factors and the ambiguity in the choice of Q^2 for the two-jet and three-jet events.

D.4 Evidence of the Running of α_s

Finally, a sampling of α_s measurements at various Q^2 values is shown in Fig. D.4. where the results discussed above have been summarized in a very naïve

fashion. We wish to determine if α_s exhibits the downward running that we expect from an $SU(3)$ gauge theory. Unfortunately, an answer to this fundamental question is not yet clear. If we disregard the quarkonium values, the trend of the data favors a running behavior, but even then a flat $\alpha_s(Q^2)$ is not ruled out. A quantitative assertion of this statement is difficult because the uncertainties in the measurements are dominated by systematic errors.

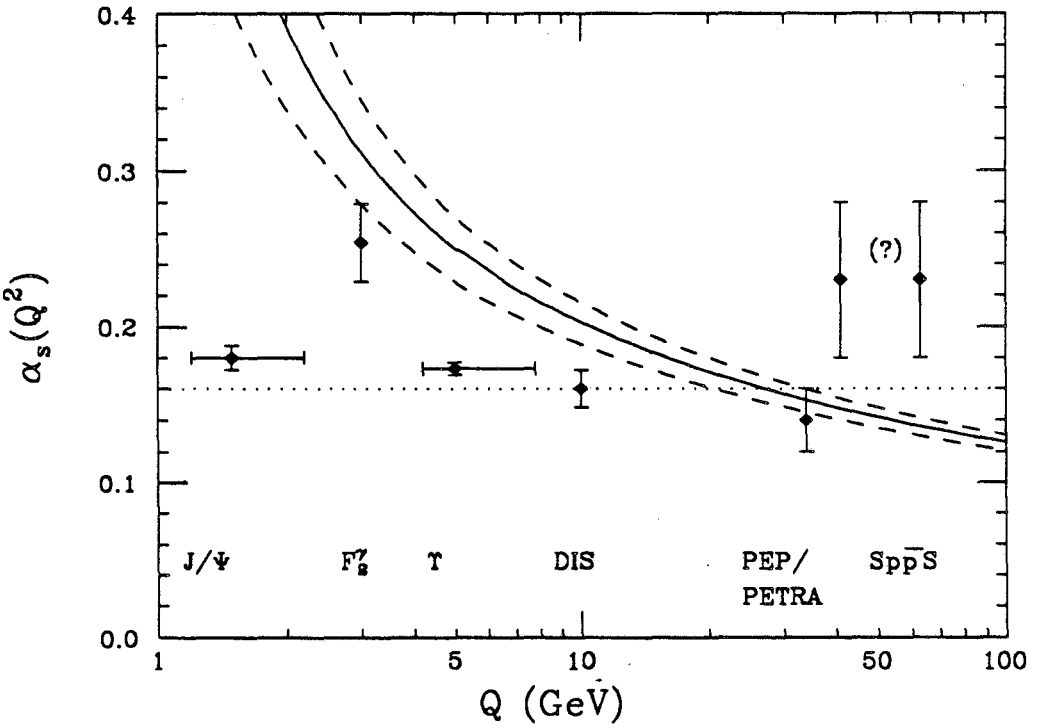

Figure D.4 α_s **measurements at different** Q^2 **values.** *The points show the various measurements discussed in this appendix. The solid curve represents the prediction of QCD if was assume the* α_s *value from the present analysis, and the dashed curves show the one-sigma limits of this prediction. The dotted line, for comparison, is an arbitrary example of fixed behavior of* α_s.

It is important to recall that direct comparisons of α_s from different processes is not necessarily justified. Consequently, some of the best studies of the running behavior of α_s come from PETRA, where the experiments examine the same observable over the range of PETRA energies. (22 GeV $\leq E_{cm} \leq$ 44 GeV).[66] The present result can only be applied to such an analysis after the Mark II has collected data at SLC energies (≈93 GeV).

REFERENCES

1. M. Dine and S. Sapirstein, Phys. Rev. Lett. **43**, 668 (1979); W. Marciano, Phys. Rev. D**29**, 580 (1984).
2. A figure showing all of the $O(\alpha_s{}^2)$ diagrams for $e^+e^- \rightarrow quarks + gluons$ can be found in D.W. Duke and R.G. Roberts, Phys. Rep. **120**, 275 (1985).
3. R.K. Ellis, D.A. Ross and A.E. Terrano, Nucl. Phys. **B178**, 421 (1981).
4. F. Gutbrod, G. Schierholz and G. Kramer, Z. Phys. **C21**, 235 (1984); K. Frabricius, G. Kramer, G. Schierholz and I. Schmitt, Phys. Lett. **97B**, 43 (1980).
5. Z. Kunstz, Phys. Lett. **99B**, 429 (1981).
6. T.D. Gottschalk and M.P. Shatz, Calt.-68-1172,-1173,-1199 (1985), unpublished, and T.D.Gottschalk, private communication.
7. T.D. Gottschalk and M.P. Schatz, Phys. Lett. **B150**, 451 (1985).
8. F. Gutbrod, G. Kramer, G. Rudolph and G. Schierholz, Z. Phys. **C35**, 543 (1987).
9. C.L.Basham, *et al.*, Phys. Rev. **D17**, 2298 (1978).
10. H.-J.Behrend *et al.*, Z. Phys. **C14**, 95 (1982).
11. H.-J.Behrend *et al.*, Phys. Lett. **B138**, 31 (1984).
12. W.Bartel *et al.*, Z. Phys. **C25**, 231 (1984).
13. M. Althoff *et al.*, Z. Phys. **C26**, 157 (1984).
14. E.Fernandez *et al.*, Phys. Rev. D**31**, 2724 (1985).
15. B. Adeva *et al.*, Phys. Rev. Lett. **54**, 1750 (1985).
16. Ch. Berger *et al.*, Z. Phys. **C28**, 365 (1985).
17. S. D. Ellis, Phys. Lett. **B117**, 333 (1982).
18. A. Ali and F. Barreiro, Phys. Lett. **B118**, 155 (1982).
19. T. Sjöstrand, Z. Phys. **C26**, 93 (1984).
20. D. Schlatter *et al.*, Phys. Rev. Lett. **49**, 521 (1982).
21. R.H.Schindler *et al.*, Phys. Rev. D**24**, 78 (1981).
22. Proposal for the Mark II at SLC, CALT-68-1015 (April, 1983), unpublished.

23. G. Hanson, Nucl. Instr. Meth. **A252**, 343 (1986).
24. W.T.Ford *et al.*, Nucl. Inst. Meth. **A255**, 480 (1987).
25. R.C.Jared *et al.*, I.E.E.E. Trans. Nucl. Sci. **N-S 33**, #1, 916 (1986).
26. J.D.Bjorken and S.J.Brodsky, Phys.Rev. **D1**, 1416 (1970); G. Hanson *et al.*, Phys.Rev.Lett **35**, 1609 (1975); we used the definition from C. Berger *et al.*, Phys.Lett **82B**, 449 (1979).
27. Our choice of bin intervals follows a convention established by CELLO[10] and followed by JADE[12] and MAC[14].
28. M.Chen and L.Garrido, Phys. Lett. **B180**, 409 (1986).
29. F.A.Berends and R.Kleiss, Nucl. Phys. **B178**, 141 (1981).
30. P.C.Rowson *et al.*, Phys. Rev. Lett. **54**, 2580 (1985).
31. T. Sjöstrand, Computer Phys. Comm. **39** (1986); T. Sjöstrand, M. Bengtsson, LU TP 86-22 (1986).
32. This is an improved version with baryon production based on A.Ali *et al.*, Phys.Lett. **93B**, 155 (1980).
33. H.M.Schellman, Ph.D. Thesis, LBL-18699 (1984), unpublished.
34. P. Hoyer *et al.*, Nucl. Phys. **B161**, 349 (1979). We implement the Hoyer scheme with the Lund symmetric fragmentation function with parameters A=1.1, B=.7, σ_q=.295 GeV.
35. A.Petersen *et al.*, Submitted to Phys. Rev. D.
36. These integrals are shown for several experiments and models in Ref. 35.
37. H. Aihara *et al.*, Z. Phys. **C28**, 31 (1985).
38. M. Althoff *et al.*, Z. Phys. **C29**, 29 (1985);H. Aihara *et al.*, Phys. Rev. Lett. **57**, 945 (1986); P.D. Sheldon *et al.*, Phys. Rev. Lett. **57**, 1398 (1986).
39. The parameters used for the Lund string model are y_{min} = 0.015, A = 0.9, B = 0.7, and σ_q=0.265 GeV/c. Parameters for the Lund Shower model are Q_0=1.0 GeV, A = 0.45, B = 0.9, and σ_q=0.230 GeV/c.
40. B. Andersson *et al.*, Phys. Rep. **97**, 31 (1983).
41. C. Peterson *et al.*, Phys. Rev. **D27**, 105 (1983).

42. S.Bethke, Z. Phys. **C29**, 175 (1985).

43. W. Bartel *et al.*, Z. Phys. **C33**, 23 (1986).

44. In this case, we define the individual n-parton rates by a y_{min} cut of 0.04.

45. B. Naroska, Phys. Rep. **148**, 67 (1987), and references therein.

46. A.Ali *et al.*, Phys.Lett. **93B**, 155 (1980). We implement the Ali scheme with the Lund symmetric fragmentation function with parameters A=.75, B=.7, σ_q=.285 GeV.

47. Proposal for the Mark II at SLC, CALT-68-1015, April, 1983.

48. W. Farr *et al.*, Nucl. Instr. and Meth. **156**, 283 (1978).

49. R.C.Jared, *et al.*, I.E.E.E. Trans. Nucl. Sci. **N-S 33**, #1, 916 (1986).

50. D. Wood *et al.*, Mark II/SLC Note #99 (1985), unpublished.

51. J. Haggerty, Mark II/SLC Note #137 (1986), unpublished.

52. W. Bartel *et al.*, Phys. Lett. **134B**, 275 (1984); *ibid.* **157B**, 340 (1985).

53. Ya.I. Azimov *et al.*, Phys. Lett. **165B**, 147 (1985).

54. R.D. Field and R.P. Feynman, Nucl. Phys. **B136**, 1 (1978).

55. B.R. Webber, Nucl. Phys. **B238**, 492 (1984)

56. T.D. Gottschalk and D. Morris, CALT-68-1365 (1986).

57. T. Sjöstrand and M. Bengtsson, LU TP 86-22 (unpublished).

58. G.P. Lepage, *Proceedings of the 1983 International Symposium on Lepton and Photon Interactions at High Energies*, 565, 1983.

59. S. Bethke, in *Proceedings of the XXIII International Conference on High Energy Physics*, 1079 (1987).

60. H.J. Behrend, *et al.*, Phys. Lett. **183B**, 400 (1987).

61. A.C. Benvenuti *et al.*, CERN-EP/87-101 (1987), submitted to Phys. Lett. B.

62. W. Wagner, *Proceedings of the XXIII International Conference on High Energy Physics*, 1227 (1987).

63. J.H. Field, F. Kapusta and L. Poggioli, *Proceedings of the XXIII International Conference on High Energy Physics*, 1232 (1987).

64. J.R. Hansen for the UA2 collaboration, *Proceedings of the XXIII Interna-*

tional Conference on High Energy Physics, 1045 (1987).

65. F. Ceradini for the UA1 collaboration, *Proceedings of the XXIII International Conference on High Energy Physics*, 1051 (1987).

66. M. Adeva etal, Phys. Lett. **180B**, 181 (1986);JADE Collaboration, reported at 1987 Lepton Photon Conference, Hamburg.

LAWRENCE BERKELEY LABORATORY
TECHNICAL INFORMATION DEPARTMENT
UNIVERSITY OF CALIFORNIA
BERKELEY, CALIFORNIA 94720